

MASTER'S THESIS 2018

**Power flow control strategies for an energy
storage in a solar powered DC microgrid**

ELIN ENHÖRNING & EMMA ODEHED

Department of Electrical Engineering
Division of Electric Power Engineering
CHALMERS UNIVERSITY OF TECHNOLOGY
Gothenburg, Sweden 2018

Power flow control strategies for an energy storage in a solar powered DC microgrid
ELIN ENHÖRNING & EMMA ODEHED

© ELIN ENHÖRNING & EMMA ODEHED, 2018.

Supervisor: Mattias Persson, RISE Research Institutes of Sweden
Examiner: Peiyuan Chen, Division of Electric Power Engineering

Department of Electrical Engineering
Division of Electric Power Engineering
Chalmers University of Technology
SE-412 96 Gothenburg
Telephone +46 31 772 1000

Cover: Dynamic controller of the system

Typeset in L^AT_EX
Printed by [Reproservice]
Gothenburg, Sweden 2018

Acronyms

AC	Alternating Current
AWL	A Working Lab
BESS	Battery Energy Storage System
EMF	Electromotive Force
DC	Direct Current
DOD	Depth of Discharge
EOL	End of Life
ESO	Energy Storage Optimiser
FED	Fossil free Energy District
FLH	Full Load Hour
GMT	Greenwich Mean Time
PV	Photovoltaic
MPPT	Maximum Power Point Tracking
PMSM	Permanent Magnet Synchronous Machine
PWM	Pulse Width Modulation
SCL	Self Consumption Level
SOC	State of Charge
SSO	Solar String Optimiser
ÅF	Aktiebolaget Ågpanneföreningen

Decision variables

n_{series}	Number of series connected battery cells	
$n_{parallel}$	Number of parallel connected battery cells	
Q_{max}	Max allowed charge and discharge rate of the battery	(W)
Q_{min}	Min required charge and discharge rate of the battery	(W)
E_{batt}	Battery storage capacity	(kWh)

Calculation variables

ΔI	DC current from the solar panels and DC load	(A)
ΔP	Power difference between generation and demand	(kW)
ΔV_{DC}	Allowed voltage variation on the DC-link	(V)
θ	Transformation angle for $\alpha\beta$ to dq -transformation	($^\circ$)
λ_{tot}	Total losses	(W)
$\lambda_{converters}$	Losses in converters	(W)
$\lambda_{battery}$	Losses in battery	(W)
$\lambda_{DC-link}$	Losses in DC-link	(W)
ρ_{avrg}	Average electricity spot price during one day from <i>Nordpool</i>	(kr/kWh)
A_{PV}	Combined area of solar panels	(m^2)
E_c	Energy in DC-link capacitor	(kWh)
E_{charge}	Energy entering the battery	(kWh)
$E_{discharge}$	Energy exiting the battery	(kWh)
E_{exp}	Energy exported to the grid	(kWh)
E_{grid}	Energy to and from the grid	(kWh)
E_{imp}	Energy imported from the grid	(kWh)
G_b	Direct beam irradiance	(W/m^2)
I_{batt}	DC current to and from the battery	(A)
I_{C1}	Current through the load side DC-link capacitor	(A)
I_{C1}	Current through the grid side DC-link capacitor	(A)
I_{DC}	DC current on the DC-link grid side	(A)
I_n	DC current through the impedance in the DC-link	(A)
i_{sd}	Real part of stator AC current in dq-coordinates	(A)
$i_{sd,ref}$	Reference for the real part of stator AC current in dq-coordinates	(A)
i_{sq}	Imaginary part of stator AC current in dq-coordinates	(A)
$i_{sq,ref}$	Reference for the imaginary part of stator AC current in dq-coordinates	(A)
k	Gradient of the V-SOC characteristics of the battery	
n_{cycles}	Number of full battery cycles per year	
P_{batt}	Power to and from the battery	(kW)
$P_{batt,ref}$	Power reference to and from the battery	(kW)
P_c	Power in DC-link capacitor	(kW)
P_{charge}	Power to the battery	(kW)
$P_{discharge}$	Power from the battery	(kW)
P_{exp}	Power exported to the grid	(kW)
$P_{exp,max}$	Max exported power to the grid	(kW)
P_{gen}	Generated solar power	(kW)
P_{grid}	Power to and from the grid	(kW)
$P_{grid,ref}$	Reference for power to and from the grid	(kW)
P_{imp}	Power imported from the grid	(kW)
P_{in}	Input power	(kW)
$P_{imp,max}$	Max imported power from the grid	(kW)

P_{out}	Output power	(kW)
V_{Batt}	Terminal battery voltage	(V)
V_{DC}	DC voltage on the DC-link	(V)
V_{DC1}	Load side DC voltage on the DC-link	(V)
V_{DC2}	Grid side DC voltage on the DC-link	(V)
V_n	Voltage across the DC-link impedance	(V)
v_α	Real part of stator AC voltage in $\alpha\beta$ -coordinates	(V)
v_β	Imaginary part of stator AC voltage in $\alpha\beta$ -coordinates	(V)
v_a	Phase a voltage in three phase system	(V)
v_b	Phase b voltage in three phase system	(V)
v_c	Phase c voltage in three phase system	(V)
v_{conv}	Converter AC voltage	(V)
v_{grid}	Grid AC voltage	(V)
v_{sd}	Real part of stator AC voltage in dq-coordinates	(V)
v_{sq}	Imaginary part of stator AC voltage in dq-coordinates	(V)

Parameters

α	Azimuth angle, south	($^\circ$)
α_{vr}	Grid current controller bandwidth	(rad/s)
α_{cr}	DC-link voltage controller bandwidth	(rad/s)
α_{crb}	Battery current controller bandwidth	(rad/s)
β	Tilt angle, angle to horizontal plane	($^\circ$)
δ	Dependent declination angle	($^\circ$)
θ_i	Incidence angle	($^\circ$)
θ_z	The angle of solar irradiance to a horizontal plane.	($^\circ$)
$\eta_{AC/DC}$	Efficiency of AC/DC converter	(%)
η_{batt}^{rt}	Round trip efficiency of battery	(%)
$\eta_{DC/AC}$	Efficiency of DC/AC converter	(%)
$\eta_{DC-link}$	Efficiency of DC-link	(%)
η_{ESO}	Efficiency of energy storage optimiser	(%)
η_{PV}	Efficiency of solar panels	(%)
η_{SSO}	Efficiency of solar string optimiser	(%)
ρ_{spot}	Hourly electricity spot price from <i>Nordpool</i>	(kr/kWh)
τ	Time constant for step response	(s)
ψ_r	Motor flux velocity constant	(Vs/rad)
ω_r	Grid frequency	(rad/s)
C	Capacitance used in the DC-link voltage controller design	(F)
C_1	Capacitance of the load side DC-link capacitor	(F)
C_2	Capacitance of the grid side DC-link capacitor	(F)
C_{DC}	Capacitance of the AC/DC converter model	(F)

f_c	Cut-off frequency	(Hz)
G	Irradiance	(W/m ²)
G_{bn}	Perpendicular direct beam irradiance to a plane	(W/m ²)
G_{bt}	Direct beam irradiance to a tilted plane	(W/m ²)
G_d	Diffuse irradiance	(W/m ²)
G_r	Reflected irradiance	(W/m ²)
G_{sc}	Solar constant	(W/m ²)
I_{MPP}	Current output at MPPT	(A)
I_{sc}	Short circuit current	(A)
L_{DC}	DC-link inductance	(H)
L_{sd}	Real part of stator inductance in dq-coordinates	(H)
L_{sq}	Imaginary part of stator inductance in dq-coordinates	(H)
n_{days}	Number of days since the 1 st of January	
P_{load}	Power consumed by the load	(kW)
P_{PV}	Power from the PV-panels	(kW)
R_a	Active damping	(Ω)
R_{batt}	Internal resistance of the battery	(Ω)
R_{DC}	DC-link resistance	(Ω)
R_s	Grid resistance	(Ω)
$SOC(t)$	State of charge of the battery	(%)
SOC_{min}	Minimum allowed charge level in the battery	(%)
SOC_{max}	Maximum allowed charge level in the battery	(%)
$V_{DC,nom}$	Nominal DC-link voltage	(V)
V_{MPP}	Output voltage at MPP	(V)
V_{OC}	Open circuit voltage	(V)
V_{SOC}	SOC dependent voltage in the battery	(V)
T_L	Turbidity factor	(%)
t_r	Rise time for step response	(s)

Logical operators

$\mathbf{A} \ \&\& \ \mathbf{B}$	$\mathbf{A} = \text{TRUE}, \mathbf{B} = \text{TRUE}$
$\mathbf{A} \ \ \mathbf{B}$	$\mathbf{A} = \text{FALSE}, \mathbf{B} = \text{FALSE}$
$\mathbf{A} \ \& \ \mathbf{B}$	$\mathbf{A} = \text{TRUE}, \mathbf{B} = \text{FALSE}$
$\mathbf{A} \ \& \ \mathbf{B}$	$\mathbf{A} = \text{FALSE}, \mathbf{B} = \text{TRUE}$

Power flow control strategies for an energy storage in a solar powered DC microgrid

Elin Enhörning & Emma Odehed
Department of Electrical Engineering
Division of Electric Power Engineering
Chalmers University of Technology

Abstract

To meet the Swedish government energy goal of increased use of renewable energy and higher consumer efficiency, a solar powered DC-microgrid with an energy storage was implemented in *A Working Lab* (AWL) in Johanneberg Science Park, Gothenburg. AWL will have 170 kW installed capacity of solar power, a 760 VDC DC-bus, a maximum load demand of 70.4 kW and an energy storage, which size is to be decided. This thesis proposes a theoretical method to optimise the size of the energy storage and to efficiently control the power flow in the building. The energy storage, consisting of a battery, was dimensioned by evaluating how various charge rates and battery sizes affected the self-sufficiency of the microgrid and its power exchange to the grid. Furthermore, two battery control strategies were implemented. The first one focuses on maximising the self-sufficiency and the second on minimising the operational cost of the system. Both strategies also aim to minimise losses, preserve battery life and to keep the power balance in the system. The optimal storage for the system was found to be a 300 kWh battery with a maximum charge- and discharge rate of 100 kW. The control strategies were successfully implemented and the system originally had a self-sufficiency of 44.9% without using any battery, but reached a significantly higher self-sufficiency prior to implementing a battery. The first strategy reached a self-sufficiency of 65.6% and the second one 59.1%. Additionally, the cost minimising strategy also resulted in a higher import of energy during low electricity price hours and a higher export of 12 MWh/year. Furthermore, a dynamic controller was implemented to investigate the dynamic response of the microgrid controller due to variations in irradiance and load. In order to investigate the dynamic response a mathematical representation of physical components was implemented in MATLAB Simulink®. Evaluation of the dynamic controller verified that the power balance in the system was kept and both the voltage and current were maintained within allowed range. The performance was deemed satisfactory for dynamic variations in loads and solar irradiance.

Keywords: DC-microgrid, Storage sizing, Self-sufficiency, Dynamic control

Acknowledgements

To, **Mattias**, our supervisor at RISE. Thank you for your solemn capitulation when we invaded your office. For knowing when to put (and for teaching us the meaning of you putting) headphones on. For decreasing your frequency of taking Jesus' sweet name in vain, and for admitting our thesis was "quite alright" in the end. All jokes aside, thank you for your support and guidance with our thesis and job hunting. Further, we also appreciated that you introduced us to so many new ways of starting an email. Your favourite was "Hepp!" but we liked "Tjolla Hopp!" better. We will use it when we keep in touch, cause we will. We know you will miss us kids too.

To **Anders**, our second supervisor at RISE. Thank you for your weariless efficiency and for giving us unarguable life hacks. Such as "There is a little place in this world for everyone." And our personal favourite: "How the actions of others make you feel can never be argued."

To **Peiyuan**, our examiner at Chalmers, Thank you for being the only professor who had a coffee with us students during the lecture breaks. For never letting on how superior you are to us and making it so easy to come to you for guidance. But most of all, thank you for always greeting us with a smile.

To **Stefan**, Simulink oracle at Chalmers, Thank you is not enough. We bow to your patience and how you made time in your busy schedule to help us. We always entered your office without a clue, but left confident in our Simulink skills.

Partners in crime

Finally we want to thank each other. Five years at Chalmers has come to an end, five years of partnership and countless hours of howling with laughter. Hopefully we can find new howling buddies at work, though we doubt they'll be half as fun.

Always remember -

When things go wrong, ask Matlab to hang on and "Recaclutale"!

And of course, tau. Never forget tau.

Elin Enhörning & Emma Odehed, Gothenburg, June 2018

Contents

List of Figures	xv
------------------------	-----------

List of Tables	xviii
-----------------------	--------------

1 Introduction	1
1.1 Background	1
1.2 Aim	1
1.3 Problem description	1
1.4 Scope	3
1.5 Limitations	3
2 Relevant theory	5
2.1 DC microgrid	5
2.1.1 Projects to demonstrate microgrids	5
2.2 Batteries	7
2.2.1 Batteries general	7
2.2.2 Lithium ion based batteries	8
2.2.3 Ageing of Lithium ion batteries	9
2.3 Solar irradiance general	9
2.3.1 Direct beam to diffuse irradiance ratio	9
2.3.2 Direct beam to a tilted plane	10
2.3.3 The impact of the earth's orbit around the sun and the seasons	10
2.4 Solar panels	11
2.4.1 Maximum power point tracking	12
2.4.2 Self-sufficiency	13
2.5 Electricity price	14
3 Realization	15
3.1 Solar irradiance data	15
3.2 Analysing irradiance data	17
3.3 Load data	18
3.4 Analysing load data	19
3.5 Battery storage sizing and operation strategies	20
3.6 Battery operation strategies	21
3.6.1 Maximise self-sufficiency	22
3.6.2 Minimise operational cost	23

4	Results on Battery Sizing and Operation Strategy	27
4.1	Sizing the battery storage	27
4.1.1	Charge- and discharge rate	27
4.1.2	Battery storage size	28
4.2	Simulation of control strategies	32
4.2.1	Increase self-sufficiency	33
4.2.2	Minimize cost	34
5	Dynamic controller	35
5.1	General system model	35
5.2	Models of physical components in Simulink®	36
5.2.1	Grid model	37
5.2.2	AC/DC converter model	39
5.3	Derived models of physical components in Simulink®	40
5.3.1	DC-link model	40
5.3.2	Deriving the battery model	41
5.4	Dynamic controllers in Simulink®	43
5.4.1	Grid current controller	43
5.4.2	DC-link voltage controller	45
5.4.3	Battery current controller	47
5.5	Validation of implemented regulators	48
5.5.1	Rise time	48
5.5.2	Power balance and losses	52
5.5.3	Manual test sequence	53
5.5.4	Increase capacitance to lower battery current peaks	57
6	Conclusions and Future work	59
6.1	Conclusions	59
6.2	Improvements and future work	60
	Bibliography	63
A	Appendix 1	I

List of Figures

1.1	System setup, with provided physical components for an internal DC-grid.	2
2.1	Equivalent circuit of a battery. The internal resistance is modeled by R_{batt} and represent the losses with each charge cycle.	7
2.2	Cross section of battery, where the electrolyte is the active material transporting electron carrying ions through the separator during charging, and returning ions during discharge.	8
2.3	Incoming light to a horizontal plane. The angle θ_z denotes the angle from the normal to the plane.	10
2.4	Incoming light to a tilted plane. The angle θ_z denotes the angle from the normal to the plane and β the tilt angle of the panel.	10
2.5	Variations of δ during the earth's orbit around the sun. Where the large, central orb is the sun and the two smaller represent the earth in orbit with six months apart.	10
2.6	Solar irradiance for one year measured on the island of Hönö.	11
2.7	Generic IV-curve for the output of a solar cell, showing current and voltage levels as well as the maximum power point.	12
2.8	Electricity prices for the 1 st of March, June, September and December in 2017 which are all working days. Prices taken from <i>Nordpool</i> area <i>SE3</i>	14
3.1	Solar irradiance measured on the island of Hönö on the 1 st of March, sampled at 100 Hz.	16
3.2	Filtering results using two different functions in MATLAB®. Unfiltered data in black, <code>filter</code> in blue and <code>filtfilt</code> in red.	17
3.3	Irradiance during sunny days, March 23 rd , June 15 th , September 27 th and December 12 th	18
3.4	Daily energy consumption by office ventilation in June.	19
3.5	Daily energy consumption by office ventilation in December.	19
3.6	Daily energy consumption by office lights in June.	19
3.7	Daily energy consumption by office lights in December.	19
3.8	Combined office loads from lights and ventilation during a working day in; March, June, September and December.	20
3.9	Maximise self-sufficiency flowchart: control strategy aiming to maximise self-sufficiency by controlling the power flow.	22

3.10	Minimising operational cost flowchart: control strategy aims to minimise operational cost by taking electricity pricing in to consideration.	24
4.1	Annual E_{exp} (solid) and E_{imp} (dashed) with different storage sizes, using Hönö data.	28
4.2	Annual E_{exp} (solid) and E_{imp} (dashed) with different storage sizes, using ÅF data.	28
4.3	The self sufficiency of the system for various battery sizes.	29
4.4	Number of battery cycles over time with a DOD of 80% for various battery sizes using Hönö data.	30
4.5	Number of battery cycles over time with a DOD of 80% for various battery sizes using ÅF data.	30
4.6	Imported and exported power each hour during one year. Using Hönö data and a battery size of 0 kWh. The dotted lines show the maximum import (-70.4 kW) and export (170.0 kW).	31
4.7	Imported and exported power each hour during one year. Using Hönö data and a battery size of 300 kWh. The dotted lines show the maximum import (-70.4 kW) and export (170.0 kW).	31
4.8	Imported and exported power each hour during one year. Using ÅF data and a battery size of 0 kWh. The dotted lines show the maximum import (-70.6 kW) and export (153.2 kW).	32
4.9	Imported and exported power each hour during one year. Using ÅF data and a battery size of 300 kWh. The dotted lines show the maximum import (-70.6 kW) and export (153.2 kW).	32
4.10	Simulations of the system during the 9 th of March, using the ideal self-sufficiency strategy.	33
4.11	Simulations of the system during the 9 th of March, using the non-ideal self-sufficiency strategy.	33
4.12	Simulations of the system during the 9 th of March, using the non-ideal self-sufficiency strategy.	34
4.13	Simulations of the system during the 9 th of March, using the non-ideal cost minimising strategy.	34
5.1	Overview of the AWL system components, used to implement Simulink [®] controllers and models of physical components.	35
5.2	Block representation of the dynamic model built in Simulink [®] . Red blocks represent implemented controllers, green blocks are mathematical models of system components and white blocks are calculation blocks. Encircled parameters represent signals to or from MATLAB [®] workspace.	36
5.3	Equivalent circuit of an AC/DC converter connected to the main grid.	37
5.4	Equivalent circuit of a PMSM in dq-coordinates, used for modeling the grid. The back EMF is denoted as $\omega_r \psi_m$.	38
5.5	The equivalent circuit for the DC-link. Used to calculate differential equations need to model the DC-link.	40
5.6	Approximation of the linear relation between V_{SOC} and SOC .	42
5.7	Overview of the cascaded control setup for the Simulink [®] implementation.	43

5.8	Schematics of the grid current controller. The index x can be exchanged for d or q to represent both signals in the dq -reference frame.	44
5.9	Equivalent circuit of the simplified DC-link previously seen in Figure 5.5, where $C = C_1 + C_2$ and $V_{DC} = V_{DC1} = V_{DC2}$.	45
5.10	Block schedule for the DC-link voltage controller, showing the inputs and outputs.	47
5.11	Block schedule for the battery current controller, showing the inputs and outputs.	48
5.12	Step response for the grid current controller for a step of 150 kW. $\alpha_{cr} = 1000$ (rad/s)	49
5.13	Step response for the battery current controller for a step of 200 A. $\alpha_{crb} = 7$ (rad/s)	50
5.14	Step response for the DC-link voltage controller for a step up to 790 V. $\alpha_{vr} = 40$ (rad/s).	50
5.15	Step response for the voltage controller with different bandwidths, $\alpha_{vr} = 40, 60$ and 80 rad/s.	51
5.16	The battery current reference, $I_{batt,ref}$ and the actual battery current, I_{batt} .	54
5.17	The alterations in SOC due to changes of the battery current, I_{batt} .	54
5.18	The power entering and exiting the battery, used to calculate SOC	55
5.19	The power reference and the actual power transferred to and from the grid.	55
5.20	The DC-link voltage reference and the actual DC-link voltage	56
A.1	The entire Simulink model used to model the AWL system. The signals in individual squares represent signals sent to MATLAB® workspace.	I
A.2	Control system containing the PWM module and current controller for the grid.	II
A.3	Current reference calculation block, for the grid current controller.	II
A.4	Grid current controller, used for regulating the current sent from the DC-link to the grid model.	III
A.5	PWM module used for calculating the duty cycle for the grid current.	III
A.6	Physical model of the AC/DC converter and the subsystem which contains the physical models of DC-link and battery.	IV
A.7	The physical models of DC-link and battery.	V
A.8	Calculation of battery SOC based on the battery current $ibatt$ and the current battery voltage $V_{batt}(SOC)$.	V
A.9	The Zero sequence block alters the common neutral point of the grid voltage.	VI
A.10	Grid model in Simulink	VI
A.11	DC-link voltage controller in Simulink	VII
A.12	Battery current controller in Simulink.	VII
A.13	The performance of the battery current controller when $C = C_1$.	IX
A.14	The performance of the battery current controller when $C = 100C_1$.	IX
A.15	The performance of the DC-link voltage controller when $C = C_1$.	X
A.16	The performance of the DC-link voltage controller when $C = 100C_1$.	X

A.17 The performance of the grid power current controller when $C = C_1$.	XI
A.18 The performance of the grid power current controller performance when $C = 100C_1$.	XI

List of Tables

1.1	System components from Figure 1.1.	2
3.1	Specifications from the two data sets used.	15
4.1	Number of full cycles per year for Hönö data and Åf data	29
4.2	The impact on grid interaction based on battery storage size, using Hönö irradiation data in an ideal system using self-sufficiency control.	30
4.3	The impact on grid interaction based on battery storage size, using ÅF irradiation data in an ideal system using self-sufficiency control.	31
4.4	Imported and exported energy for two cases of self-sufficiency control strategy, ideal and non-ideal.	33
4.5	Imported and exported energy from two non-ideal control setups, maximise self-sufficiency and minimise cost.	34
5.1	Parameters for grid model in dq-reference system.	39
5.2	Parameter for the AC/DC converter model.	39
5.3	Parameters of the DC-link model.	41
5.4	Calculations of battery model parameters.	42
5.5	Parameters of grid current controller	44
5.6	Parameters for the DC-link voltage controller.	46
5.7	Parameters for the battery current controller.	47
5.8	Initial conditions for all dynamic simulations	48
5.9	Bandwidth and rise time for the three implemented controllers	51
5.10	Validation strategy for the dynamic controllers. The total simulation time is 3 s.	53
A.1	Validation strategy for dynamic controllers. Total simulation time is 3s.	VIII

1

Introduction

1.1 Background

In 2008 the Swedish government presented a new energy goal to increase the use of renewable energy and to improve the efficiency of energy use in Sweden. By 2020 a minimum of 50% of the total energy consumption should come from renewable energy sources and the energy efficiency should be increased by 20% [1]. Simultaneously, solar panels has increased in efficiency and due to the drastic decrease in cost, solar power is growing throughout the world [2]. This price change in combination with the development of energy storage, presents an interesting possibility for small scale, self-sufficient systems. Additionally, the interest in DC-grids on end user level has been a driving force for research. Having DC, instead of AC on end user level, can result in up to 5% higher efficiency [3] due to lower conversion losses. In Gothenburg, Akademiska hus are utilizing these opportunities in the construction of a new building, "*A Working Lab*" (AWL) [4]. The new office building will serve as a Working Lab, where companies can lease research integrated offices. The roof will be covered in PV-panels which, together with a battery storage, will power lighting and ventilation for certain parts of the building via an internal DC-grid. The remaining loads will run on AC and be powered from the main grid.

1.2 Aim

The main aim for this thesis is to control the power flow in AWL, using control strategies focusing on minimise the operational cost or maximise the self consumption, as well as determine the optimal size of a battery storage. Additionally a dynamic controller of the system will be simulated to investigate the consequences of fast variations in loads and solar irradiance.

1.3 Problem description

The DC-grid inside the building will be powered by 572 roof top solar panels on AWL and also from the neighbouring building, resulting in an installed capacity of 170 kW. Additionally, a Battery Energy Storage System (BESS) with the capacity $100 < E_{batt} < 500$ kWh will be installed to increase the utilization of solar. Lights and ventilation are the main DC-loads in the building, remaining loads will be fed from the main AC-grid. Figure 1.1 show a system setup where all the components

in the system are presented. The efficiency values in Figure 1.1 are presented with further information in Table 1.1.

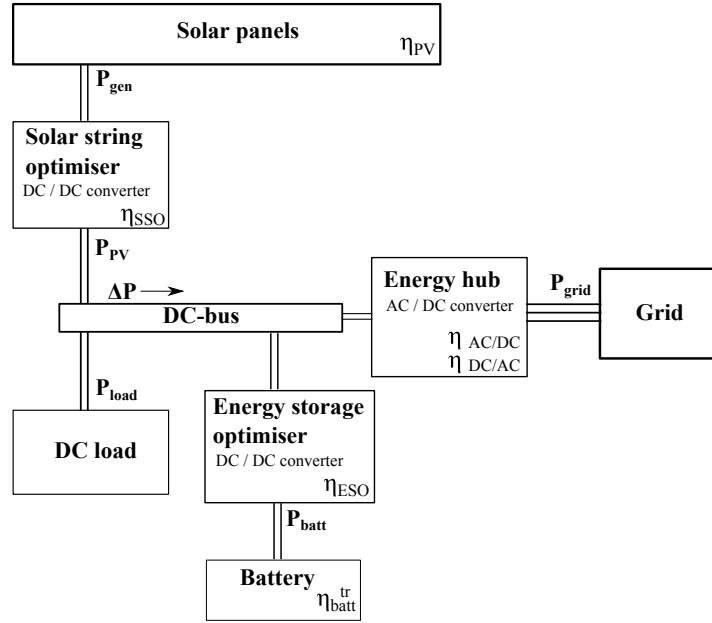


Figure 1.1: System setup, with provided physical components for an internal DC-grid.

Table 1.1: System components from Figure 1.1.

System components	Function	Levels	Efficiency
Solar panels	Energy producer	170 (kW)	$\eta_{PV} = 0.17$ [5]
Solar string optimiser (SSO) DC/DC converter	Perform maximum-power point tracking DC/DC conversion	≈ 6 (kW)	$\eta_{SSO} = 0.99$ [6]
Energy Hub AC/DC converter DC/AC converter	Control DC-link voltage AC/DC conversion DC/AC conversion	≈ 28 (kVA) ≈ 28 (kVA)	$\eta_{AC/DC} = 0.98$ [6] $\eta_{DC/AC} = 0.985$ [6]
Energy storage optimiser (ESO) DC/DC converter	Control battery-terminal voltage DC/DC conversion	≈ 6 (kW)	$\eta_{ESO} = 0.99$ [6]
Battery pack DC bus	Energy storage Internal DC grid	100-500 (kWh) 760 ± 40 (VDC)	$\eta_{batt}^{rt} = 0.94$ [6] $\eta_{DC-link} \approx 1$

The solar string optimiser, energy hub and energy storage optimiser presented in Table 1.1 are provided by the company Ferroamp [6] and the efficiencies were given during a meeting [7]. The battery efficiency is taken from a Ferroamp battery, however the actual battery to be used in AWL is not yet decided.

1.4 Scope

Solar irradiance data from Chalmers measurement setup at Hönö is used in this thesis project. It is collected at an horizontal angle of $\beta = 45^\circ$ and an azimuth angle of $\alpha = 185^\circ$ south. Even though the solar panels are to be placed in other directions and angles on AWL, this will not be taken into consideration. This will affect the result as the sensor placement is optimal for solar exposure in Sweden, but the panel placement is not. The resulting power output will then be lower in the real system than in these simulations.

All data such as irradiance, power market prices and demand peak hours are based on Swedish conditions. This means that the irradiance will decrease during the winter months, when electricity prices and loads will increase due to colder weather and higher demand. This means that there are varying circumstances throughout the year. Hence, the control strategies will need to be altered before being used in another country with another geographical location. Closer to the equator for example, the irradiance, electricity prices and load characteristics are less dependent on season. In those cases other control strategies are needed.

Since the generated solar power, P_{PV} , will be an input to the controller. The purpose is not to model the solar panels per say, but merely to model the output power. The controller should function regardless of input and thus neglecting the origin of power and the equivalent circuit of the solar panels will have a minor impact on the controller performance.

1.5 Limitations

The limitations in this project are presented in the nine following bullet points.

- As the irradiance data is measured during one year, the result will only reflect this year. Even though the exposure of sunlight is the same year after year, the weather is not. Therefore the resulting generated power would have been different should another years data had been used.
- The irradiance data is collected by a sensor monitoring an area that is considerably smaller than the total solar panel installation area. However, the irradiance registered on the sensor surface will be assumed to be uniformly distributed over the panel installation area. This will affect the result in a negative way, as one small cloud can shade the sensor, but for the PV installation there might still be unshaded panels. Hence, the power output from the real system is estimated to be higher than in this thesis.
- The AWL building was still under construction during the entire thesis project, the loads were therefore not yet known. To be able to perform the simulations in this thesis, estimations of the office loads on hourly basis were provided by ÅF. Due to not being able to measure the actual load in AWL, dynamic variations cannot be detected. Instead a mean value for each hour will be

used. This will affect the instantaneous result but the annual simulated results should not stray too far from the actual values.

- Cost minimising means that during operation, the purchasing price for the battery is not included. This simplification is done as the most cost efficient solution would be to not purchase a battery at all at the moment of this work.
- Battery life preservation will be assumed to be done best by following the recommendations and guarantees from battery manufacturers. The recommended Depth of Discharge (DOD) will be followed so that the battery is limited to stay between a certain SOC_{min} and SOC_{max} each cycle.
- For all simulations run over several years the irradiance, pricing, battery performance and loads are assumed to be equal for each year.
- Losses in cables in the system are not considered in the simulations done when using the hourly sampling frequency.
- The allowed variation range of state of charge in the battery is set to 10-90% and is not varied in the simulations. This results in a DOD of 80% of the battery size.
- All simulations start at the 1st of January and the initial state of the battery is at SOC_{min} . This will affect the possibility to reach 100% self-sufficiency, regardless of battery size, as the solar irradiance during Swedish winter is not enough to sustain both the load and store for later use.

2

Relevant theory

Chapter 2 presents relevant theories for a better understanding of Chapter 3, 4 and 5. It contains theories regarding microgrids, solar irradiance, solar panels and electricity price. All sections are adapted in the following three chapters.

2.1 DC microgrid

In 2012 the U.S Department of Energy defined microgrids as:

“a group of interconnected loads and distributed energy resources within clearly defined electrical boundaries that acts as a single controllable entity with respect to the grid. A microgrid can connect and disconnect from the grid to enable it to operate in both grid-connected or islandmode.” [8]

Today, microgrids are growing in appearances and due to their ability to lower losses they are beneficial to consumers and grid operators [9]. They are constructed in different sizes, designed for different power levels and are applicable for DC, AC and also for the combination of them both in a hybrid microgrid. In DC microgrids the energy resources and loads are connected to a common DC bus. Similarly, an AC microgrid uses a common AC bus. Besides higher efficiency, another benefit is the possibility to use a microgrid as a stand-alone unit, in so called islanding operation. In already grid connected places this offers a chance to be more self-sufficient by generating some of the own power demand. However, in places surrounded by tough terrain or remote islands, having access to a local microgrid might be the only solution for power supply.

All three categories of microgrids can supply both AC and DC loads using converters but in the comparison between AC and DC microgrids, DC microgrids offer several advantages [9]. Reduction of AC/DC conversion stages offers a higher system efficiency and benefit from integration of energy sources such as PV. Furthermore, the increasing numbers of DC loads in electronic devices, energy storage and electric vehicles also favour DC microgrids.

2.1.1 Projects to demonstrate microgrids

Most of the recent DC microgrid projects are utilized to demonstrate the use and value of DC distribution systems and microgrid control. The over all benefits, efficiency improvements and cost reduction between AC and DC systems are often the

main focus. Following projects were implemented in order to demonstrate this.

1. **Fraunhofer Institute, Erlangen, Germany**

Fraunhofer Institute has built a grid connected DC powered office building test bed. The system has a 380 VDC DC bus and a smaller 24 VDC nanogrid for lighter electronic loads. Further, the system includes DC lighting, EV chargers and a battery storage. The energy savings for the DC system ranged between 2.7% to 5.5% compared to an equivalent AC system [3].

2. **Xiamen University, China**

The College of Energy at Xiang'an Campus implemented DC microgrid with 380 VDC on the DC bus. The generation of the system is a 150 kW PV system and the load consist of 30 kW DC air conditioning, 40 kW DC electric car charging station and a total of 20 kW DC LED lighting. The system also have a small (200 Ah 336 VDC) lead acid storage system and a AC/DC back up unit. An analysis showed that the performance of this system could be increased with a properly dimensioned storage system and that hybrid microgrids are more suitable for commercial buildings instead [10].

3. **Bosch DC microgrid, California, US.**

Bosch developed and implemented several DC microgrids in order to compare the performance with equivalent AC grids. In 2016 the company installed a DC microgrid platform in Honda Motors distribution center in Chino California [11]. The system included a 300 kW solar PV and 5540 kWh of energy storage. The biggest DC loads of the system is, 120 kW of LED lighting and 111 industrial ceiling fans possible to run on DC and adapting speed after the instantaneous PV generation. Further, 12 fork-lift chargers are connected, possible to charge the fork-lifters but also to use as energy storage backup in cases of grid outage or for peak load shaving [12].

4. **Coconut Island Microgrid , Hawaii, US.**

The marine research laboratory on Coconut island has several critical loads and high energy reliability needs. The grid on the island is a hybrid microgrid, supplying both AC and DC loads in the facilities. The systems peak demand is approximately 500 kW and it has currently 200 kW of PV and small scale wind turbines installed. For emergency occasions the power flow control is expected to perform load-shedding and the system also has two emergency diesel generators. The energy storage systems on the island consist of fuel cells and batteries. It is expected to run in 2018 [13].

2.2 Batteries

This section, discusses basic theory, equivalent circuit and aging of a battery. It is important to remember that batteries have losses, the roundtrip efficiency of a charge cycle is less than 100%. It is therefore beneficial to store excess energy in the battery after supplying the load.

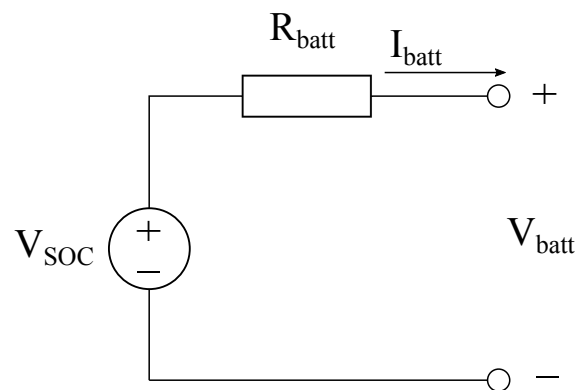


Figure 2.1: Equivalent circuit of a battery. The internal resistance is modeled by R_{batt} and represent the losses with each charge cycle.

The losses within the battery can be simplified as one internal resistance, R_{batt} , as shown in Figure 2.1. The voltage source, V_{SOC} is dependent of the state of charge (SOC) in the battery and is bigger for a higher SOC. V_{batt} is the terminal voltage of the battery and I_{batt} is the battery current.

2.2.1 Batteries general

Batteries are available in various sizes and shapes, the four main components anode, cathode, electrolyte and separator. During charge the electrons are transported by active carrier ions, from the cathode through the separator and are bound to the anode material. During discharge the potential difference between the anode and cathode drive a current to supply a connected load. The electrons separate from the ions and once they are positively charged again, they are drawn back to the negative cathode.

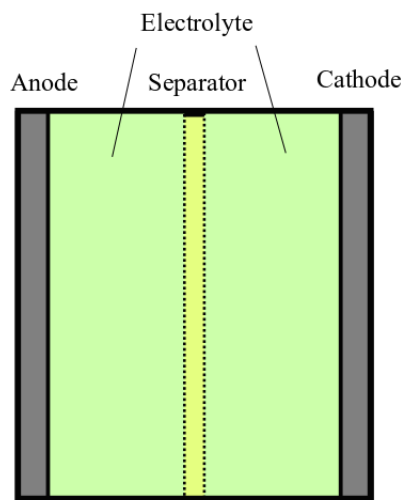


Figure 2.2: Cross section of battery, where the electrolyte is the active material transporting electron carrying ions through the separator during charging, and returning ions during discharge.

Figure 2.2 show the schematics of a battery, where the separator divides the electrolyte into anode and cathode parts, still allowing the electron carrying ions to pass through. As the chemical reactions occur on the surface of both anode and cathode material, the four main components are made thin and twirled close together, prior to casing.

2.2.2 Lithium ion based batteries

One of the most common batteries today use lithium as active material. Besides the benefit of having only one carrier material, as oppose to Ni-Cd batteries, li-ion batteries have higher energy density compared to other rechargeable batteries on the market [14]. When charged, negative ions carrying electrons enter the graphite anode and attach via intercalation. This means the ions do not disturb the structure of the anode material, but take place inside the hollow hexagon spaces in each sheet of graphene. Once the battery is discharged, the electrons are released and the now positive ions travel back through the separator to the cathode, back to the cathode side through the separator. The energy density in a li-ion battery depends on the material used in the anode and the amount of electrolyte. However, dense graphite layers yield a dense energy storage, but limits the mobility of the electrons. Resulting in a high energy but low power battery, as the charge and discharge rate is lower than for spacious graphite structure. One reason why the lithium batteries is the most used in the car industry is the high performance of the batteries [15]. Other reasons are the fact that li-ion batteries can be utilized in a large scale and their ability to endure increased depth of discharge (DOD) and a higher number of cycles than lead-aid based batteries [16].

2.2.3 Ageing of Lithium ion batteries

The high cost of a battery storage could be a significant part of any installation cost, vehicle or stationary power system [17]. Therefore, is the life expectancy of the battery of high interest. The ageing of a li-ion battery can be divided into *calendar ageing*, which depend on time of usage, and *cycle ageing*, depending on the amount of usage. Within the *cycle ageing* the degradation is affected by the state of charge (SOC), DOD, withdrawn current and temperature. However, a generic model of ageing is very complex to predict [18]. Battery manufacturers generally state a guaranteed number of cycles to a certain DOD before the battery reaches its end of life (EOL). However, EOL is more important for the electric vehicle industry than for stationary installations as it affects the driving range of the vehicle. Stationary batteries are in comparison with a vehicle battery often used for smaller DOD in each cycle. Car batteries can still be utilized in for example PV installations past their due date and are then called second-life batteries.

2.3 Solar irradiance general

To determine the amount of solar irradiance hitting a roof mounted solar panel, three kinds of irradiance must be taken into account. The global irradiance G , is defined as

$$G = G_b(\theta) + G_d + G_r \quad (2.1)$$

where G_b is the direct beam irradiance, G_d is the diffuse irradiance and G_r the reflected irradiance. The individual parts of (2.1) are hereby explained. G_b is the radiation whose angle of incidence from the sun is perpendicular to the panel surface. It depend on the time of day, horizontal angle of the panels, as well as coordinates and azimuth angle. G_d is radiation scattered by particles in the air on the way through the atmosphere and hence hit the panel from any direction. Therefore it depends on the air quality and pollution rate. Finally G_r is radiation reflected off the ground and on to the panel. Naturally this component depends on the reflectivity of the solar panel surroundings and is much lower for a field than for snow or water [19].

2.3.1 Direct beam to diffuse irradiance ratio

The ratio of direct beam to diffuse irradiance on to a horizontal plane depend on the scattering of light through the atmosphere and can be written as

$$G_{bn} = G_{sc} e^{-\frac{T_L}{0.9+9.4\cos(\theta_z)}} \quad (2.2)$$

[19], where G_{sc} is the solar constant, a flux density measuring mean solar irradiance per unit area. T_L is the turbidity factor, a measurement of pollution in the air affecting the irradiance hitting the panel. T_L tend to be higher in urban areas and lower on high altitudes where the air is cleaner. θ_z is the zenith angle, the angle between the zenith and the centre of the sun's horizontal plane.

2.3.2 Direct beam to a tilted plane

For incoming irradiance perpendicular to the solar panel, the incidence angle, θ_i , is 0° , for a horizontal plane, the angle is instead dependent on the zenith angle of the sun. Hence G_b , is found as

$$G_b = \cos(\theta_z)G_{bn} \quad (2.3)$$

where G_{bn} is the direct irradiance normal to the plane. For a tilted solar panel at an angle β , the relationship between the incoming irradiance and the direct beam, is calculated as

$$G_{bt} = \cos(\beta) G_{bn} = \frac{\cos(\beta)}{\cos(\theta_z)} G_b. \quad (2.4)$$

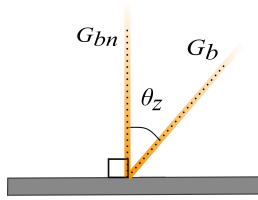


Figure 2.3: Incoming light to a horizontal plane. The angle θ_z denotes the angle from the normal to the plane.

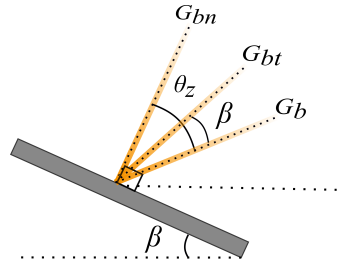


Figure 2.4: Incoming light to a tilted plane. The angle θ_z denotes the angle from the normal to the plane and β the tilt angle of the panel.

2.3.3 The impact of the earth's orbit around the sun and the seasons

The tilt of the earth's axis vary between 23.45° and -23.45° compared to the sun. This creates a time dependent declination angle, δ , of irradiance hitting the surface of the earth throughout a year.

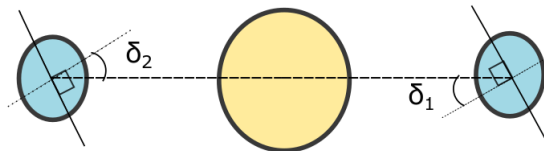


Figure 2.5: Variations of δ during the earth's orbit around the sun. Where the large, central orb is the sun and the two smaller represent the earth in orbit with six months apart.

When the earth orbits around the sun, δ is the angle between the earth's axis and a line normal to the radius between the center of the earth and the center of the sun. Figure 2.5 shows the changes in δ , where δ_1 and δ_2 represent the earth's position, six months apart. Simplified, δ can be found as

$$\delta = 23.45^\circ \sin\left(360^\circ \frac{284 + n_{days}}{365}\right) \quad (2.5)$$

n_{days} denotes the n^{th} day since the start of the year, so that the 1st of January is represented by $n_{days} = 1$. This is insignificant during a single day, but throughout a year it has a big impact. The variation in solar irradiance is shown in Figure 2.6.

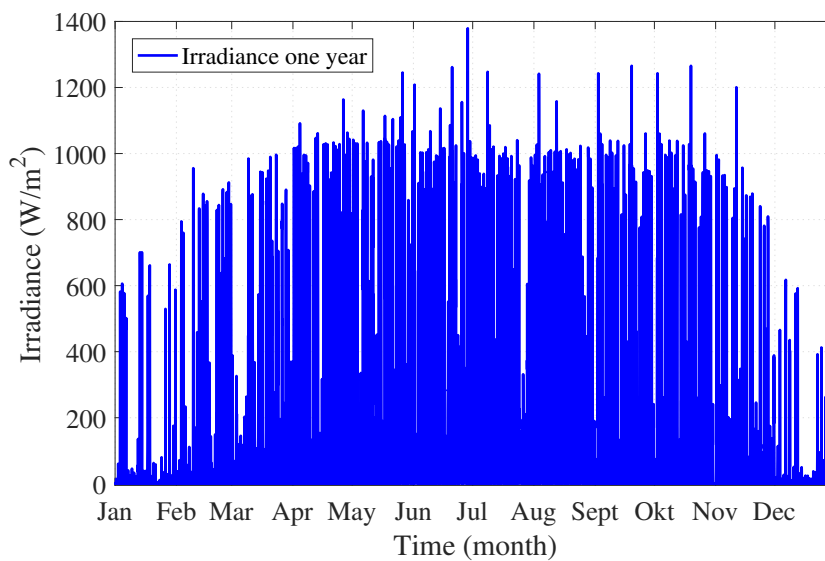


Figure 2.6: Solar irradiance for one year measured on the island of Hönö.

Figure 2.6 demonstrates the annual change in irradiance at the island of Hönö, Sweden. Worth noting is that the amplitude of the irradiance spikes are high during spring and autumn but occur more frequent during the summer months. Another factor is that the earth orbits in an ellipse and not a perfect circle around the sun. This in combination with the tilt of the axle yields that the angular velocity of the earth is not constant. This irregularity also affects the seasonal change in solar irradiance on a specific geographical location.

2.4 Solar panels

Today solar panels are constantly growing in appearance and with the decreasing price solar panels opens possibilities to provide electricity to urban areas [20]. The combination of solar panels and DC-microgrids offer an effective solution to decrease the conversion losses and increase the efficiency of the generated power [9]. The power generated by the solar panels is given by

$$P_{gen} = G A_{PV} \eta_{PV} \quad (2.6)$$

where A_{PV} is the combined area of the solar panels, η_{PV} is the panel efficiency and G is calculated from (2.1).

2.4.1 Maximum power point tracking

The output current and voltage from a solar cell has an exponential dependence. Hence, there is a combination of voltage and current values which correspond to the maximum output power.

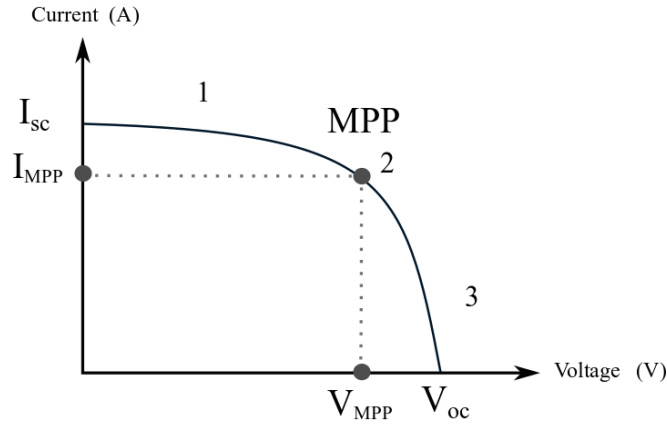


Figure 2.7: Generic IV-curve for the output of a solar cell, showing current and voltage levels as well as the maximum power point.

The maximum outputs of current respectively voltage are called the short circuit current, I_{sc} , and the open circuit voltage V_{oc} respectively. However, these values does not correlate to the maximum power point, or MPP, as can be seen in Figure 2.7. Instead these values are denoted as I_{MPP} and V_{MPP} . The MPP can be found using various methods. One of the most common methods is the Incremental Conductance [21], or IncCond, and uses the global maximum for each irradiance level on a power voltage curve. By measuring the output voltage and power from a solar cell, and finding deviations in the MPP can be identified by knowing that

$$\begin{cases} \frac{dP}{dV} > 0 & \text{prior to MPP, 1} \\ \frac{dP}{dV} = 0 & \text{at MPP, 2} \\ \frac{dP}{dV} < 0 & \text{after MPP, 3.} \end{cases} \quad (2.7)$$

The power generated by solar panels is

$$P_{gen} = V \cdot I, \quad (2.8)$$

so that (2.7) can be expressed as

$$\frac{dP}{dV} = \frac{d(VI)}{dV} = I \frac{dV}{dV} + V \frac{dI}{dV} = I + V \frac{dI}{dV} \approx I + V \frac{\Delta I}{\Delta V} \quad (2.9)$$

and can be rewritten as

$$\begin{cases} \frac{\Delta I}{\Delta V} > -\frac{I}{V} & \text{prior to MPP, 1} \\ \frac{\Delta I}{\Delta V} = -\frac{I}{V} & \text{at MPP, 2} \\ \frac{\Delta I}{\Delta V} < -\frac{I}{V} & \text{after MPP, 3.} \end{cases} \quad (2.10)$$

Meaning it tracks the MPP by evaluating the change in conductance in the output power and comparing it to the current value.

2.4.2 Self-sufficiency

The self-sufficiency or self consumption level (SCL) of a system answers to how much of the total load is supplied by self-generated energy. SCL is calculated from

$$SCL = \left(1 - \frac{\sum P_{imp}}{\sum P_{load}}\right) \cdot 100, \quad (2.11)$$

where the percentage of the imported power represent the shortage of energy in the system. A system where maximum load and maximum generation occur simultaneously, such as office buildings, are more likely to have a high SCL and make use of as much as possible of the generated energy. Any energy storage in the system is also beneficial for a high SCL or to store energy and supply loads with self-generated energy during shortage of electricity.

2.5 Electricity price

The electricity price depends on demand, availability, weather and season.

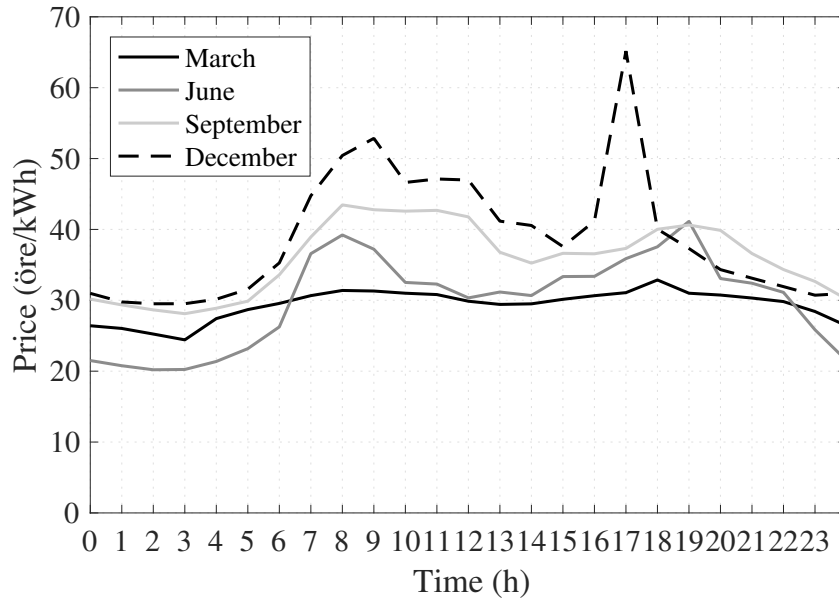


Figure 2.8: Electricity prices for the 1st of March, June, September and December in 2017 which are all working days. Prices taken from *Nordpool* area *SE3*.

As seen in Figure 2.8 the pricing differs a lot for each month and also depends on the time of a day. Figure 2.8 shows the variations in electricity spot prices in Sweden, [22] The electricity hourly spot prices for the next day are published at 13.00 every day on *Nordpool* [23]. This information opens the possibility to minimise the cost by buying energy during low price hours. It is clear from Figure 2.8 that the price is lower in March and June compared to September and especially December. Which is not preferable when using PV since the production is highest during summer and lowest during winter when the electricity price is high.

3

Realization

Each sub task in the project will be initiated by a literature study during which relevant articles and theses will be read. Prior to implementing the controller and sizing the battery, load and irradiance data must be processed. Irradiance data will be filtered and downsampled to match the load data, which is given on hourly basis. One year worth of load, and irradiance samples will then be used to simulate and evaluate the annual system behaviour. To investigate the dynamic performance and transient behaviour of the system, a continuous time model will be built in MATLAB Simulink[®].

3.1 Solar irradiance data

Two data sets of irradiance were available, one from Chalmers measurement setup at Hönö, the other simulated and provided by ÅF. Both data sets span a whole year, but the measured data is sampled at a frequency of 100 Hz, whereas the simulated once every hour. A comparison between both data sets will be done, to display how different solar panel placements and shading affect the system performance. For this comparison, the Hönö data was downsampled to hourly values.

Table 3.1: Specifications from the two data sets used.

Dataset	Hönö, "ideal"	ÅF, realistic
Azimuth angle, α	185°	160°
Tilt angle, β	45°	15°
Sampled at	100 Hz	Once an hour
Handles shading	No	Yes
Type of data	Measured	Simulated

As can be seen in Table 3.1, different tilt and azimuth angles are used for the various data sets. The irradiance sensor on Hönö is placed at 185° south, with a horizontal angle of 45°, close to the ideal angle for Gothenburg, which is 41° [24]. In ÅF's simulations, the panels are seated on a model of the AWL house in Johanneberg Science park. therefore the angles are less favourable, 160° south and tilted to only 15° to avoid shading the panels in the row behind. The measured data has more

optimal placement, due to this and the neglect of shading the measured irradiance will be higher than the simulated. In addition, the calculations of solar power using the Hönö data is modelled by linearly scaling of the sensor measurements. Hence the sunlight hitting the sensor is assumed to be uniform across the entire surface covered by solar panels. therefore, the measurements show results of shading of the sensor, all the panels in the system model will be shaded. This will affect the annual result with more days with high power generation for Hönö than for ÅF. To show a comparison between Hönö and ÅF data, both will be used in the battery sizing and hourly strategies.

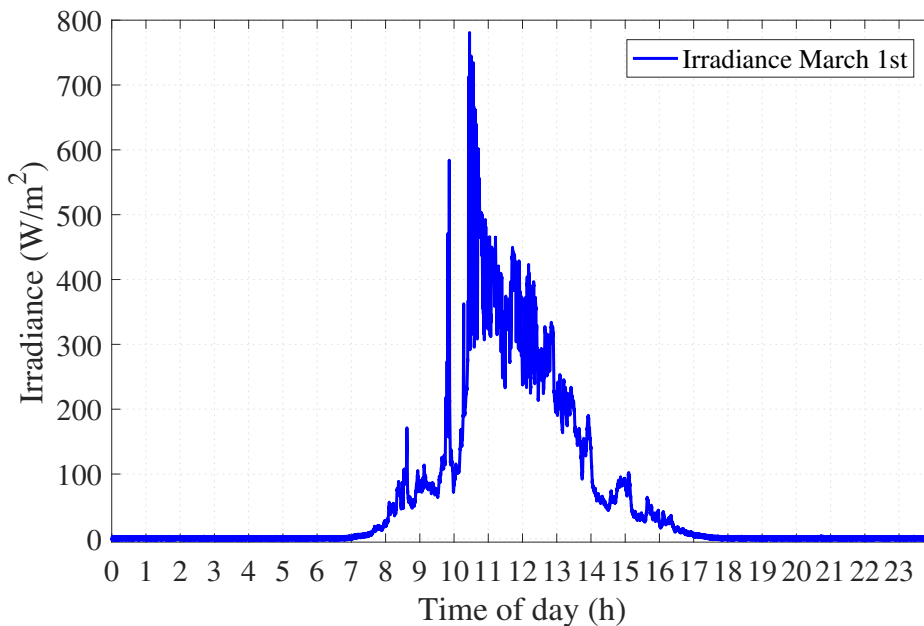


Figure 3.1: Solar irradiance measured on the island of Hönö on the 1st of March, sampled at 100 Hz.

Due to the high resolution and swift changes in the measured irradiance data, it required filtering prior to downsampling. To directly downsample the unfiltered data would present a risk of picking extreme values and not acquire a good approximation of the irradiance. Figure 3.1 shows the unfiltered irradiance data during the first of March. Note the swift change at 10:00 and the continuous variations in the measured irradiance from 11:00 to 13:00. Although irradiance may change rapidly, the simulations will be performed on hourly basis. Three different filtering functions were evaluated in MATLAB[®]. First the data was smoothed using `lowess` function, which is based on locally weighted linear regression [25]. The function calculates an average value based on the data points inside a specified interval.

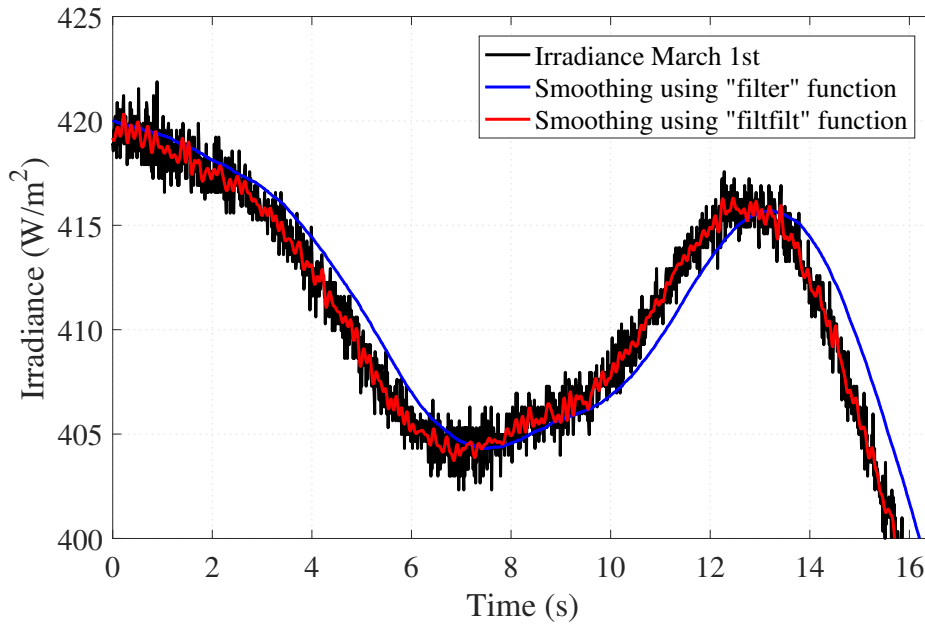


Figure 3.2: Filtering results using two different functions in MATLAB[®]. Unfiltered data in black, `filter` in blue and `filtfilt` in red.

Although the result was satisfactory, the computational time was three hours. therefore the functions `filter` and `filtfilt` were evaluated as a comparison. Figure 3.2 shows the results, where the `filtfilt` function, by visual comparison, showed the better result. This function evaluates the data in both forward and reverse direction, which eliminate the phase shift which can be seen in the curve filtered by the the `filter` function. Even though the `filter` gave a smother curve, the forward shift will cause errors in future simulations and is therefore unusable. The curve using the `filtfilt` function is still considerably less noisy than the original and is used to simulate the power generation from the solar cells on hourly basis. This curve was then down sampled and used as the measured data in all hourly simulations.

3.2 Analysing irradiance data

In order to evaluate the storage capacity needed for AWL, both the generation of solar power and the DC-system load power demand must be determined. To calculate the generation of solar power irradiance data from Chalmers measurement setup on the island of Hönö and data provided by ÅF will be used. The data set from ÅF was simulated using the software *PVsol* which uses average irradiance values of gathered data from a 22 year period from 1988 to 2010.

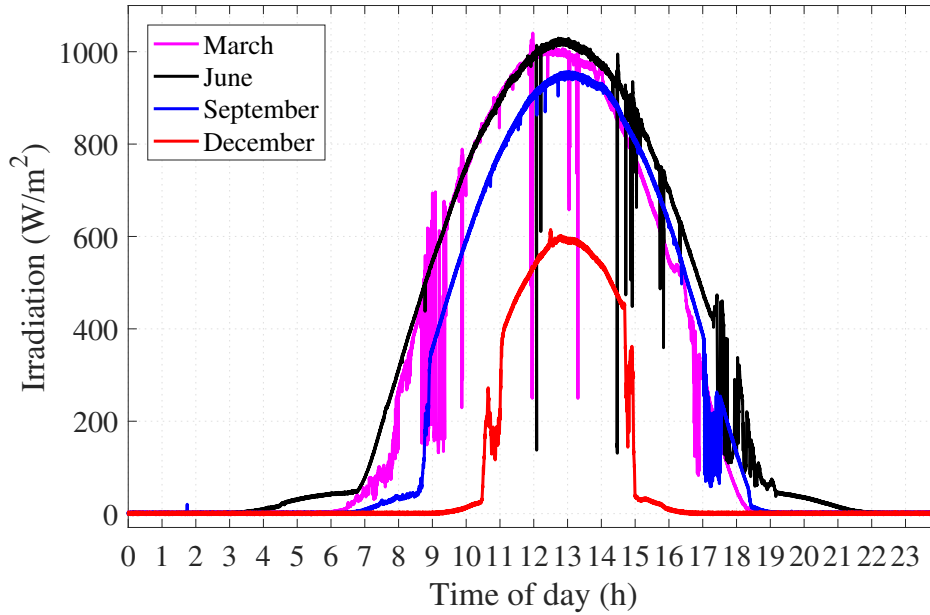


Figure 3.3: Irradiance during sunny days, March 23rd, June 15th, September 27th and December 12th.

The variations in irradiance during one day and for different seasons of the year can be seen in Figure 3.3. The irradiance in December is considerably smaller than in June. One can also note the small difference in amplitude between March, June and September, where the peaks are fairly similar. However, the solar energy throughout the day is given by the integration of each curve, and is therefore highly dependent on the daily duration of sunshine as well. All of the generated power cannot be utilized by the system load, as there will be losses in the power electronics connecting the panels to the system DC-link, the SSOs. Therefore, the usable part of the generated power (P_{PV}) can be written as

$$P_{PV} = P_{gen} \eta_{SSO}, \quad (3.1)$$

where η_{SSO} is the efficiency of the SSO, and P_{gen} is the total generated power from the solar panels.

3.3 Load data

Data for ventilation and lighting load in an office environment were provided by ÅF. The load data set is like the irradiance data simulated and sampled on hourly basis. This data is an estimate of the total load of the system and are shown in the following figures consisting of data from March, June, September and December. The office lights are daylight controlled, meaning they will consume less energy during Swedish summer. Their estimated load is approximately 45 kW at peak hours, and

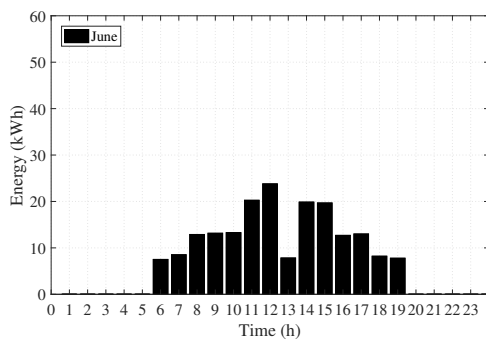


Figure 3.4: Daily energy consumption by office ventilation in June.

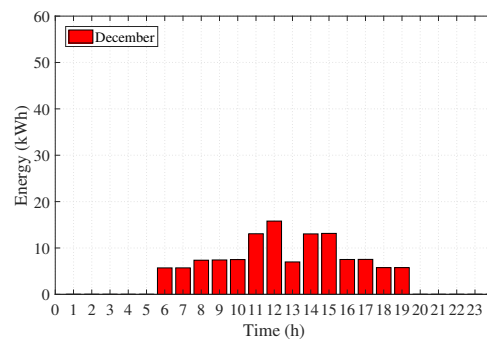


Figure 3.5: Daily energy consumption by office ventilation in December.

1.7 W outside of opening hours. The ventilation load show less annual variation, as it depends on how many employees are estimated to be in the office.

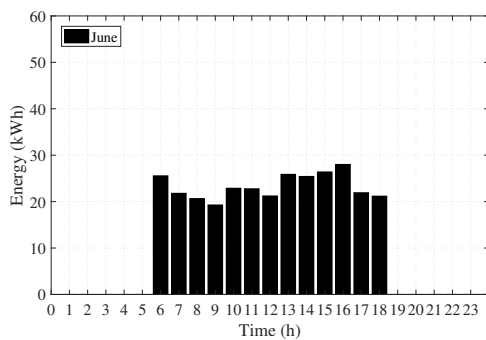


Figure 3.6: Daily energy consumption by office lights in June.

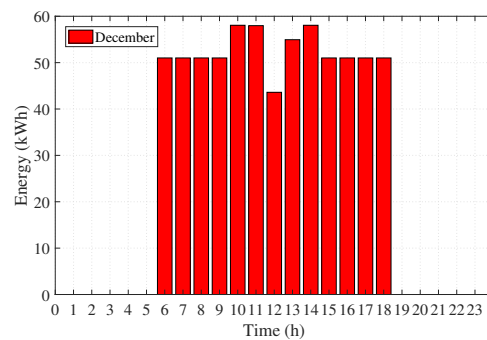


Figure 3.7: Daily energy consumption by office lights in December.

Figure 3.4 show the energy consumption of ventilation during a work day in June and Figure 3.5 a work day in December. The higher demand of ventilation in June is due a warmer climate which require temperature regulation in the building. The load from office lights in June and December can be seen in Figure 3.6 and Figure 3.7 respectively. The higher midday peaks in December is due to the increased demand for office lighting during winter set by the daylight controlled lighting.

3.4 Analysing load data

The load characteristics indicate the office energy consumption, but also the required discharge rate of the future battery storage. This, if the battery should be able to supply the load during one sample period in case of no generation from the solar panels.

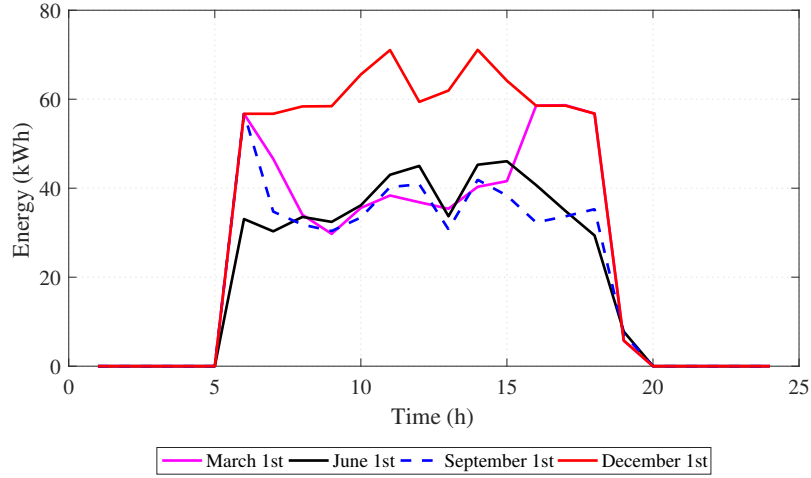


Figure 3.8: Combined office loads from lights and ventilation during a working day in; March, June, September and December.

Figure 3.8 shows a comparison of how the combined load from lights and ventilation vary during 24 hours in above mentioned months. Here, the load consist of both lights and ventilation and it can be seen how the power consumption differ for each month and over time of day, depending on the activity or control of ventilation on the office. Worth noting is that the varying energy consumption will require that the minimum charge and discharge rate, Q_{min} , is set to highest demand. Such that

$$Q_{min} = \max(P_{load}) \quad . \quad (3.2)$$

This is necessary to be able to supply the full load on days with insufficient solar power generation. The largest load of the system is found to be 71.4 kW, it occurs at 14.00 on the 11th of November. To be able to supply the load at all times, the minimum required discharge rate is 71.4 kW.

3.5 Battery storage sizing and operation strategies

The battery storage is an important component in the AWL building, as it provides larger flexibility of power usage. Excess solar power, or power purchased from the grid, can be stored and used later. The battery storage can assist the solar panels and increase self-sufficiency, this has economic benefits as it enables AWL to increase the utilization of the solar panels and purchase grid power more strategically. However, battery storage is still very expensive and has losses with every charge cycle. The charge cycle efficiency is affected by the age and chemical composition of the battery [14], as well as the battery current. In order to find the optimal storage size for AWL,

P_{PV} and P_{load} characteristics during a whole year must be taken into account. As the annual peak power demand does not coincide with the peak power generation, an optimal storage during winter is much bigger than during summer. Different strategies for the use of the battery storage can be formulated and these strategies will affect the required battery size.

3.6 Battery operation strategies

To evaluate the annual behaviour of the system while keeping the power balance, simulations will be done using hourly sample rate and three different control strategies:

- Maximise self-sufficiency
- Minimise operational cost

Both strategies are constrained to preserve battery life by utilizing the battery within certain SOC limits. Generally, batteries show the longest lifetime when DOD is kept at low percentage [14]. However, setting a low *DOD* might call for a need for a larger storage capacity as a smaller percentage of the battery is used. The concept of battery aging is still under investigation and scientists have not yet agreed on a model. therefore it will be assumed that charging and discharging to the, according to the manufacturer, specified DOD limits is the best way to preserve battery life. During all simulations it is also assumed that the battery price increases linearly with the size, and that irradiance and load data is the same with respect to year. The same data will be used multiple times to simulate several years. The excess or deviation of power in ΔP is compensated for by controlling the import or export of power to the grid and to or from the battery. Keeping the power balance in the system is considered a constraint used in both control strategies. Additionally, the losses in the system are minimised in both control strategies. To minimise the losses the controller should route the power in the most efficient way. The main loss components in the system are the DC-link losses ($\lambda_{DC-link}$), the battery losses ($\lambda_{battery}$) and the converter losses ($\lambda_{converters}$). A summation of the losses in one year results in the total loss in the system λ_{tot} .

$$\sum_{k=0}^{8760} \lambda_{tot} = \sum_{k=0}^{8760} \lambda_{DC-link} + \sum_{k=0}^{8760} \lambda_{battery} + \sum_{k=0}^{8760} \lambda_{converters}$$

Since the component with the highest loss in this system are the battery with the DC/DC converter and the AD/DC converter (see Figure 1.1 and Table 1.1), charging the battery with grid power should be avoided. The efficiency of the imported power from the grid, through the battery and to the load ($\eta_{grid \rightarrow battery \rightarrow load}$) can be expressed as

$$\eta_{grid \rightarrow battery \rightarrow load} = \eta_{AC/DC} \cdot \eta_{ESO}^2 \cdot \eta_{batt}^2$$

and results in a efficiency of 0.90. The most efficient use of the solar power would be to always supply the load with just the right amount. The variation in irradiance and

load will result in both excess and deficiency of power in the system. To minimise the losses in the system the controller can be constrained to never charge the battery with grid power, only with solar power. This implementation to minimise losses is treated as a constraint, and is used in both control strategies.

3.6.1 Maximise self-sufficiency

In the prospect of creating an autarkic system, maximising the self-sufficiency means reducing the power import and export from the main grid. Hence,

$$\text{Maximise self-sufficiency} = \text{Minimise grid interaction}$$

Minimising the interaction with the grid also eliminates the losses from the AC/DC converter while taking most use of the battery, which means all three constraints mentioned in Section 3.6 are met.

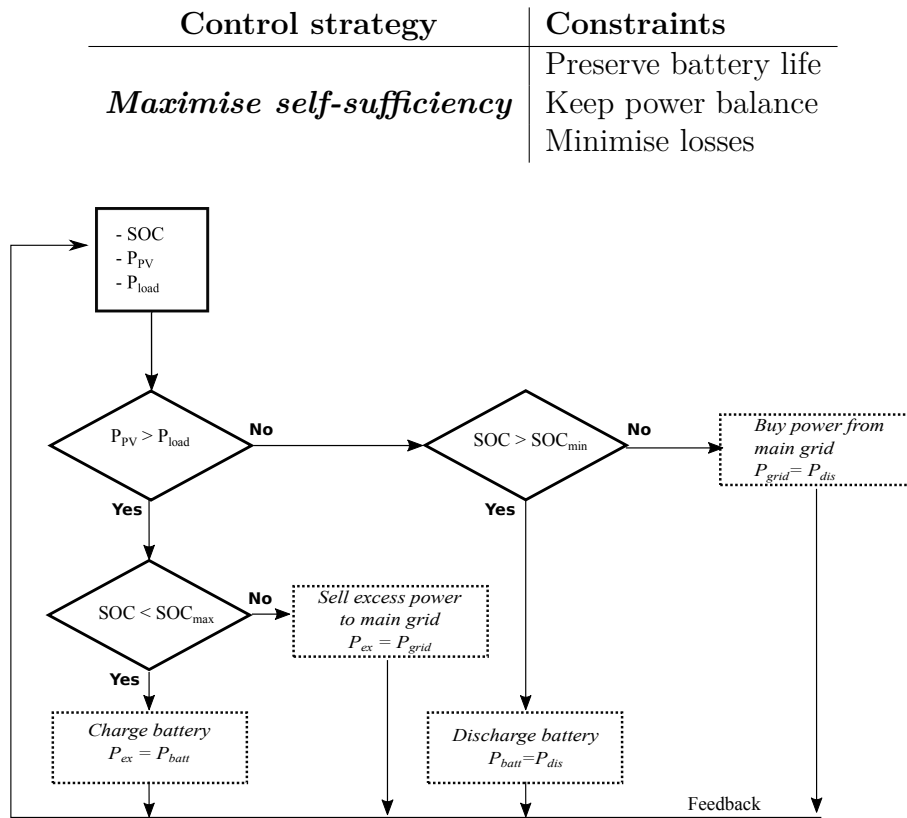


Figure 3.9: Maximise self-sufficiency flowchart: control strategy aiming to maximise self-sufficiency by controlling the power flow.

Figure 3.9 shows how the controller takes SOC , the power generation P_{PV} and the load demand P_{load} as inputs. P_{PV} and P_{load} are then compared to create ΔP . If the power generation exceeds the consumption, ΔP is positive. If the consumption is higher than the generation ΔP is negative. The deviation of power is primarily

balanced by the battery, then assisted by the grid. By limiting the use of the battery to

$$SOC_{min} < SOC(t) < SOC_{max}$$

and using only solar power to charge the battery both constraints mentioned above are met. Figure 1.1 show the power flow of the system. The controller will utilize the stored battery energy if the load demand is higher than the solar power input. Only when $SOC(t) = SOC_{min}$ will the controller purchase power from the grid. Thus, when

$$(P_{PV} > P_{load} \ \&\& \ SOC < SOC_{max}) \longrightarrow \Delta P = P_{batt},$$

ΔP is used to charge the battery, as long as it is not fully charged. Once the battery is full and the power generation still exceeds the consumption, ΔP is sold to the main grid. So that,

$$(P_{PV} > P_{load} \ \& \ | \ SOC < SOC_{max}) \longrightarrow \Delta P = P_{grid}.$$

If the power consumption exceeds the generation, and the SOC level is above minimum, the deficiency of power is compensated for by discharging the battery. Which results in,

$$(P_{PV} > P_{load} \ \& \ | \ SOC > SOC_{min}) \longrightarrow P_{batt} = -\Delta P,$$

as long as the battery does not discharge to SOC_{min} . If then the power generation still does not meet the load demand, and $SOC = SOC_{min}$, the deficiency of power is compensated by purchasing power from the main grid. Meaning,

$$(P_{PV} > P_{load} \ \|\ \ SOC > SOC_{min}) \longrightarrow P_{grid} = -\Delta P.$$

3.6.2 Minimise operational cost

As in the self-sufficiency strategy, the three constraints must also be included in this strategy.

Control strategy	Constraints
<i>Minimise operational cost</i>	Preserve battery life
	Keep power balance
	Minimise losses

Additionally, grid power market prices must be taken into account. Charging the battery with grid power is avoided, but grid imports to supply the load can be cost efficient during certain hours of the day. As electricity is cheap during night time and expensive during mornings and evenings [22], the aim is to minimise import during high price-hours.

$$\text{Operational cost} = \text{cost of electricity import}$$

If the load demand is higher than the PV generation, the controller should balance with either battery power or import from the grid, depending on the electricity price. An average price, ρ_{avg} , is calculated using

$$\rho_{avg} = \frac{\sum_{k=1}^{24} \rho_{spot}(k)}{24}. \quad (3.3)$$

Where $\rho_{spot}(k)$ is the hourly spot price every hour, k . ρ_{avg} is then compared to the spot price every hour to decide whether the current price is high or low. Hours when the price is lower than the average, are considered as *buy-time* and the controller should then purchase power rather than discharging the battery.

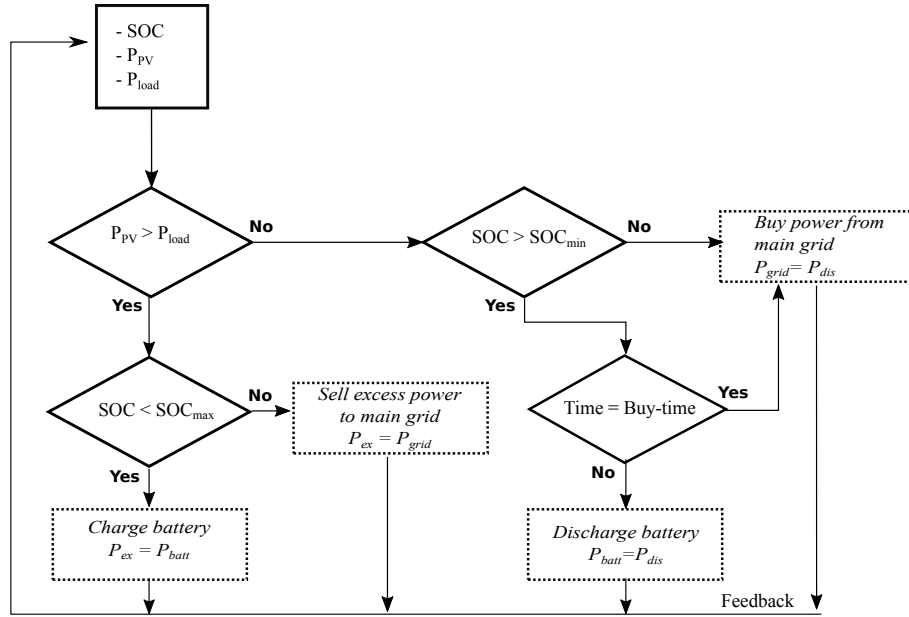


Figure 3.10: Minimising operational cost flowchart: control strategy aims to minimise operational cost by taking electricity pricing in to consideration.

The flowchart in Figure 3.10 show the working principles of the control strategy, with the added control for cost. The block controlling whether it is "buy-time" represent the decision taken after the electricity pricing was considered. The other controller inputs are P_{load} , P_{PV} and SOC . When ΔP is positive, the controller will take the same actions as in Section 3.6.1. When ΔP is negative, and enough charge in the battery such that,

$$(P_{PV} > P_{load} \mid \& \quad SOC > SOC_{min}),$$

the origin of the balancing power depend on the grid price. Resulting in that if,

$$\begin{cases} price_{spot} < price_{avg} & -\Delta P = P_{grid} \\ price_{spot} > price_{avg} & -\Delta P = P_{batt}. \end{cases}$$

Should there be no charge left in the battery, grid power is imported,

$$(P_{PV} > P_{load} \quad || \quad SOC > SOC_{min}) \quad \longrightarrow \quad -\Delta P = P_{grid}.$$

regardless of price. Having grid price as an added control input should enable more cost efficient use of the battery storage.

4

Results on Battery Sizing and Operation Strategy

In this chapter the method and hourly simulation results of the system will be presented. During each hour, the irradiance and load will be assumed to be constant. As each sample is the average value of the present hour, this method gives a good overview of the system and can be used to test control strategies and vary battery properties. All simulations will be done using MATLAB[®], irradiance data from both Hönö and ÅF, and load data from ÅF. The control strategies for maximised self-sufficiency and minimising cost will be combined with implemented and evaluated. Each simulation starts on the 1st of January, with the battery at SOC_{min} . Based on the simulation results the sizing and charge rate of the battery storage will be decided. The system annual performance will then be evaluated again to see how the chosen battery size and charge rate affect the annual power import and export.

4.1 Sizing the battery storage

To determine the required battery storage size charge rate and aim of system operation must be taken into consideration. Based on control strategy, the optimal battery size will differ. The system therefore needed to be simulated using both control strategies and both data sets separately. The results of annual export and import for energy, as well as peak power to and from the system had to be compared.

4.1.1 Charge- and discharge rate

When designing the system components, an important aspect is the charge and discharge rate, Q_{max} , of the battery, as this will affect the power flow.

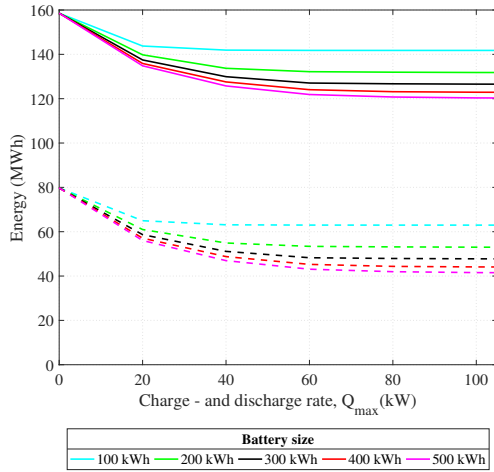


Figure 4.1: Annual E_{exp} (solid) and E_{imp} (dashed) with different storage sizes, using Hönö data.

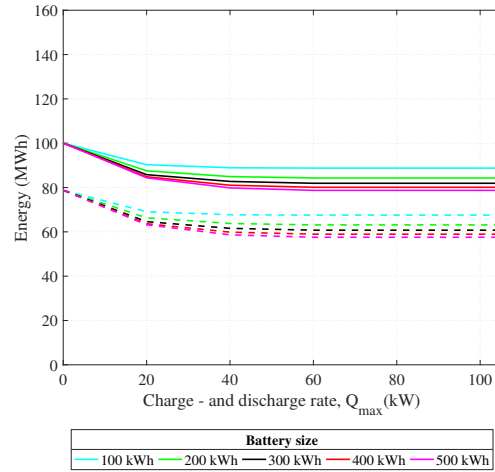


Figure 4.2: Annual E_{exp} (solid) and E_{imp} (dashed) with different storage sizes, using ÅF data.

The impact of different rates of Q_{max} and battery sizes on transferred energy can be seen in Figure 4.1 and Figure 4.2. For all simulations in this chapter, the charge rate of the battery is the same as the discharge rate. It should be noted that $E_{exp,Hönö}$ is larger than $E_{exp,ÅF}$ and that $E_{imp,Hönö}$ is smaller than $E_{imp,ÅF}$, as a result of the more favourable panel placement. Further, the grid interaction is unchanged for $Q_{max} > 60$ for ÅF data and 80 for Hönö data. Meaning that the grid interaction is then indifferent to charge rate, but more determined by the battery size and ΔP . Generally, ΔP is lower than Q_{max} the majority of times. Therefore, regardless of battery size and rate, E_{imp} , E_{exp} , and thereby also the SCL , is determined by ΔP . Based on these findings, a rate of 100 kW was chosen for the battery. There is little to no change in SCL based on different storage sizes for $Q_{max} > 90$ kW. Additionally, a higher Q_{max} enables better utilization of the generated solar power during occasional peaks. Such peaks could occur when the sun breaks through a cloud, causing a rapid change of irradiance.

4.1.2 Battery storage size

As mentioned in Chapter 3, the optimal battery size, E_{batt} , is a compromise between having a high self-sufficiency and a low cost. Figure 4.3 shows how the self-sufficiency increase by increasing E_{batt} for both data sets of irradiance.

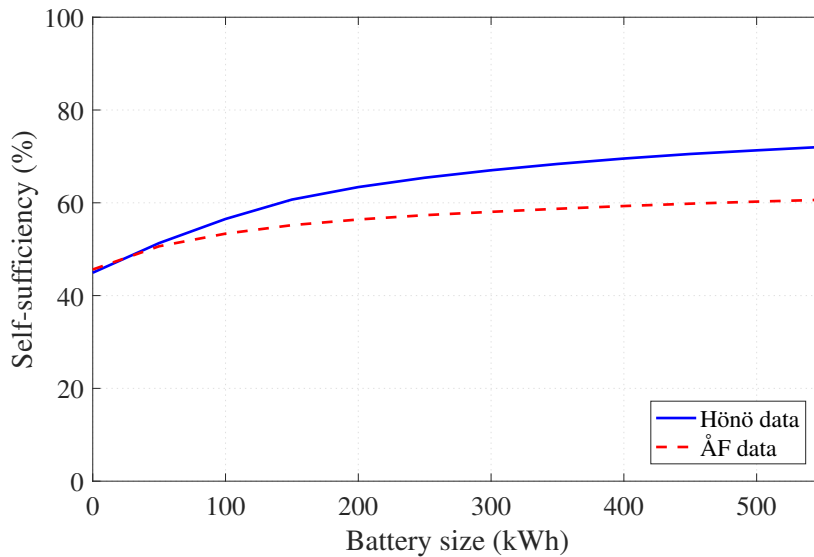


Figure 4.3: The self sufficiency of the system for various battery sizes.

Again, Hönö gives a better result, but what is most significant is that there appears to be a limit in SCL for both data sets when E_{batt} approaches 500 kWh. For Hönö the limit is almost 80% and for ÅF just over 60%. For both data sets the increase in SCL is most prominent between 100 – 300 kWh, indicating that a larger battery storage makes a small difference for the system in terms of being autarkic. An important factor for cost minimising is the life expectancy of the battery. Using hourly data to simulate the ideal system for a whole year, while limiting the DOD to 80%, the number of full cycles per year, n_{cycles} , was determined as

$$n_{cycles} = \frac{E_{charge} + E_{discharge}}{2 \cdot DOD}. \quad (4.1)$$

For this simulation, only the cycle life ageing was taken into consideration and that of calendar aging was neglected. Additionally, the annual irradiance was assumed to be repeated each year, resulting in a linear aging.

Table 4.1: Number of full cycles per year for Hönö data and Åf data .

Battery size (kWh)	Data set	100	200	300	400	500
Cycles per year	Hönö data	209	167	133	111	95
	ÅF data	140	97	75	62	53

As seen in Table 4.1 the number of cycles per year decrease with increasing battery size. The energy content in the battery is larger and more energy is required to reach a full cycle. Further, the number of cycles from 0 – 100 years was calculated to find the life time of the battery.

4. Results on Battery Sizing and Operation Strategy

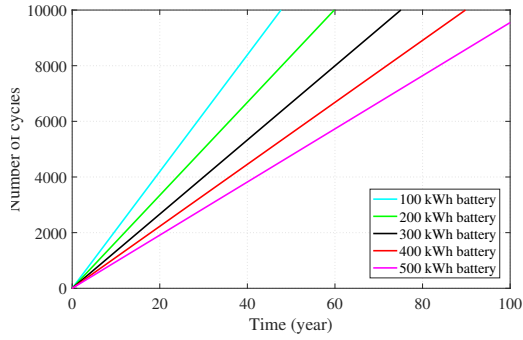


Figure 4.4: Number of battery cycles over time with a DOD of 80% for various battery sizes using Höno data.

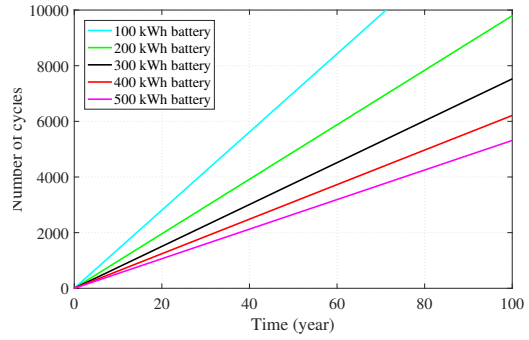


Figure 4.5: Number of battery cycles over time with a DOD of 80% for various battery sizes using ÅF data.

The result for Höno data is shown in Figure 4.4 and for ÅF data in Figure 4.5. The number of cycles using Höno data is significantly higher than for ÅF data, which again is due to the higher P_{PV} and self-sufficiency, which can be seen in Table 4.2 and Table 4.3, along with the annual energy results. The Höno data based, ideal system uses the full range of the battery more frequent as there is more power to store. In return, the grid exchange is lower and the system is more self sufficient. However, the investment price will be higher. Purchasing a 300 kWh battery storage with a guaranteed number of cycles of for example 3000, gives an expected life span of ≈ 22 years and ≈ 40 years for Höno and ÅF data respectively. It is reasonable to think that the markets of both batteries and solar panels will look very different in just a few years time. Purchasing a battery to last roughly the same time as the solar cells is therefore a good idea. Then the whole system can be re-dimensioned after 20 years.

Table 4.2: The impact on grid interaction based on battery storage size, using Höno irradiation data in an ideal system using self-sufficiency control.

Battery size	(kWh)	0	100	200	300	400	500
$\sum E_{imp}$	(MWh)	79.8	63.0	53.0	47.8	44.1	41.6
$\sum E_{exp}$	(MWh)	158.6	141.8	131.8	126.6	122.9	120.4
$P_{imp,max}$	(kW)	70.4	70.4	70.4	70.4	70.4	70.4
$P_{exp,max}$	(kW)	170.0	170.0	170.0	170.0	170.0	170.0
SCL	(%)	44.9	56.5	63.4	67.0	69.5	71.3

Table 4.3: The impact on grid interaction based on battery storage size, using ÅF irradiation data in an ideal system using self-sufficiency control.

Battery size (kWh)		0	100	200	300	400	500
$\sum E_{imp}$ (MWh)		78.8	67.6	63.1	60.8	58.9	57.6
$\sum E_{exp}$ (MWh)		100.0	88.8	84.3	81.9	80.1	78.7
$P_{imp,max}$ (kW)		70.6	70.6	70.6	70.6	70.6	70.6
$P_{exp,max}$ (kW)		153.2	153.2	153.2	153.2	153.2	153.2
SCL (%)		45.6	53.4	56.4	58.1	59.3	60.3

Table 4.2 and Table 4.3 show the total imported and exported power from the system, how big the SCL is and the maximum imported and exported instantaneous power. Note the small difference in self-sufficiency between the two data sets, increasing E_{batt} from 100 to 300 kWh gives an increase of almost 20% for Hönö, but only 11% for ÅF. Due to the lower irradiation utilization caused by the tilt angle, β , and shading of the panels. Worth noting is the fact that implementation of a battery increase the self-sufficiency significantly. Comparing the resulting self-sufficiency for a battery size of 0 kWh and 300 kWh an improvement of 22.9% for Hönö data and 12.5% for ÅF were determined using the ideal self-sufficiency strategy. Indicating that a battery storage is beneficial when trying to improve the self-sufficiency of this system.

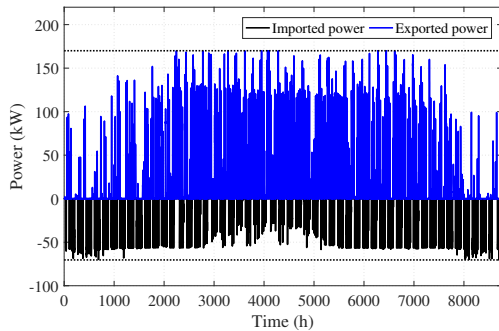
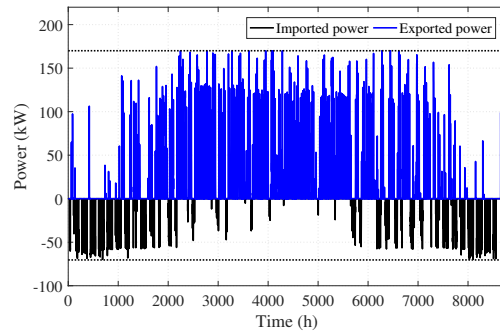
**Figure 4.6:** Imported and exported power each hour during one year. Using Hönö data and a battery size of 0 kWh. The dotted lines show the maximum import (-70.4 kW) and export (170.0 kW).**Figure 4.7:** Imported and exported power each hour during one year. Using Hönö data and a battery size of 300 kWh. The dotted lines show the maximum import (-70.4 kW) and export (170.0 kW).

Figure 4.6 and 4.7 show the power export and import for a battery of size 0 and 300 kWh simulated with Hönö data. Both figures clearly show that the export power reaches the maximum of 170 kW at several occasions during the year. Indicating that there are days when the solar panels generate rated power while the load is low. It is seen in table 4.2 that the maximum export power is the same for all battery sizes. The imported power is much lower in Figure 4.7 and indicates that the system during summer months is close to 100 % self-sufficient.

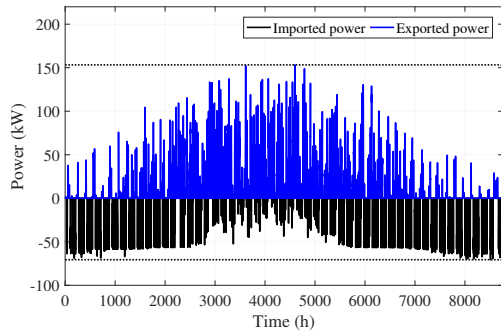


Figure 4.8: Imported and exported power each hour during one year. Using ÅF data and a battery size of 0 kWh. The dotted lines show the maximum import (-70.6 kW) and export (153.2 kW).

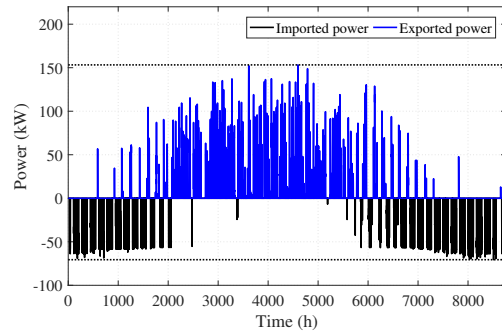


Figure 4.9: Imported and exported power each hour during one year. Using ÅF data and a battery size of 300 kWh. The dotted lines show the maximum import (-70.6 kW) and export (153.2 kW).

Figure 4.8 and 4.9 show the exported and imported power using ÅF data. Note that the maximum export power is lower than in Figure 4.6 and 4.7. This is also visible in Table 4.2 and 4.3 and the difference is again due to the difference in irradiance for the two data sets. Dimensioning of the cables connecting the system to the main grid must be made to withstand 170 kW, although it rarely is necessary to export this amount of power. To minimize losses it could be a good idea to look into sharing the excess power to other loads during these times and dimension the cables after the max load demand instead. Another alternative could be to adjust the MPPT, although this would be an inefficient use of the installed solar capacity. Based on these results it can be seen that the self-sufficiency is more dependent on battery size for sizes smaller than 300 kWh. Indicating there are less incentives to invest in a larger storage. Combined with the expensive purchase price per kWh, 300 kWh is a good compromise between the cost and self-sufficiency of the system. One could argue that the investment price for a 300 kWh battery storage is very high for an increase of self-sufficiency from 45-78%, or 45-62%. However, AWL is a research project and thus the installation is not purely for economical reasons. As a result, the most reasonable, autarkic choice is made so that $E_{batt} = 300$ kWh.

4.2 Simulation of control strategies

In this subsection, the simulation results of both suggested control strategies from section 3.7, maximised self-sufficiency and minimised cost, are presented. All simulations are made in Matlab using hourly data from both data sets and using the results from the battery size: $Q_{max} = 100$ kW and $E_{batt} = 300$ kWh, as argued in previous section. Additionally, the initial state of the battery is at SOC_{min} .

4.2.1 Increase self-sufficiency

First, the ideal system was simulated using the control strategy for maximised self-sufficiency to evaluate the chosen battery storage and charge rate. During the 9th of March the system experienced both deficiency and excess of power, which enabled a good evaluation of the control strategies. All simulations were performed over a full year, but the graphical comparison is shown using the 9th alone.

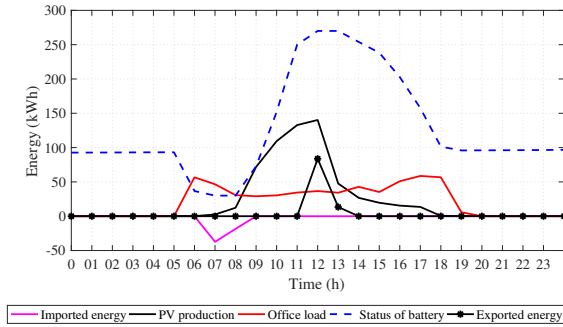


Figure 4.10: Simulations of the system during the 9th of March, using the ideal self-sufficiency strategy.

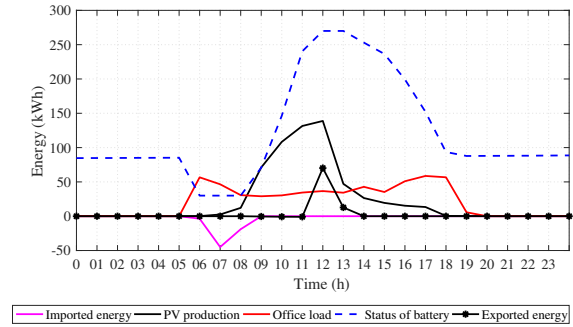


Figure 4.11: Simulations of the system during the 9th of March, using the non-ideal self-sufficiency strategy.

The ideal strategy for self-sufficiency is shown in Figure 4.10 and the non-ideal in Figure 4.11. The impact of losses in the system can be seen in Figure 4.11, for example at 07 : 00, where the import is larger than in Figure 4.10. At 12 : 00 the exported power is ≈ 60 kW in Figure 4.11, compared to ≈ 80 kW in Figure 4.10, also showing the effect of losses in the system. It is notable again at 18 : 00 where the battery discharges to ≈ 90 kWh for the non-ideal system, compared to 100 kWh during the ideal simulation. Generally, the system require a larger amount of imported power, and there is less excess power to export. The same is true for the battery, less power can be utilized in each cycle due to the non-ideal roundtrip efficiency.

Table 4.4: Imported and exported energy for two cases of self-sufficiency control strategy, ideal and non-ideal.

Control setup		Ideal self-sufficiency	Non-ideal self-sufficiency
$\sum E_{imp}$	(MWh)	47.8	49.
$\sum E_{exp}$	(MWh)	126.8	120.3
SCL	(%)	67.0	65.6

The differences in annual power export and import, and self-sufficiency is presented in Table 4.4. Note the 2% loss of SCL due to losses and keep it in mind during Section 4.3.2. where the results of minimised cost will be displayed.

4.2.2 Minimize cost

In this strategy the main focus is minimising the amount of purchased power during peak price hours. The controller compares the current grid price to the average price that day. The aim is to prevent purchasing from the grid during hours when the price is above average. Again, the day used to compare is the 9th of March, but now the non-ideal self-sufficient strategy is compared to a non-ideal cost minimising strategy. The results are shown in Figures 4.12 and Figure 4.13.

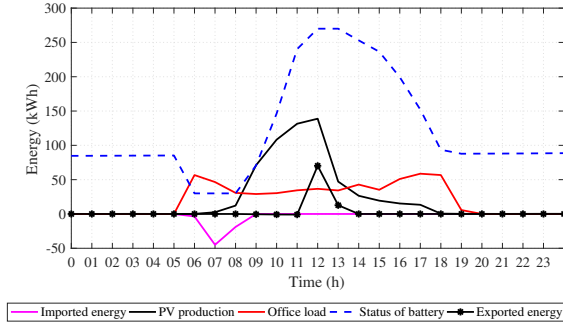


Figure 4.12: Simulations of the system during the 9th of March, using the non-ideal self-sufficiency strategy.

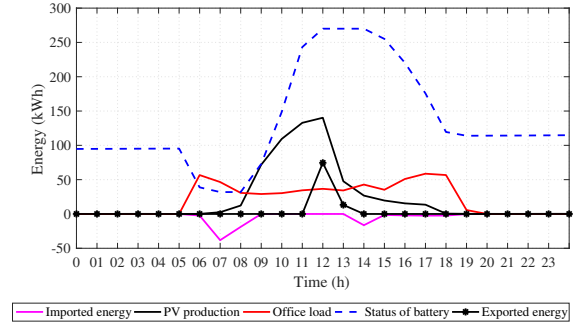


Figure 4.13: Simulations of the system during the 9th of March, using the non-ideal cost minimising strategy.

In Figure 4.13 an extra import of power can be seen at 14 : 00, even though there is available power in the battery. Due to the low grid price, the controller imports power and as a result the energy content in the battery is higher than in Figure 4.12. One can also note that the DOD at 6 : 00 is deeper in Figure 4.12 than in Figure 4.13, it reaches the SOC_{min} . The deeper discharge results in a slower increase of SOC. The utilization of the battery is higher in Figure 4.12, hence the battery ends the day on a lower level of charge.

Table 4.5: Imported and exported energy from two non-ideal control setups, maximise self-sufficiency and minimise cost.

Control setup		Non-ideal self-sufficiency	Non-ideal cost minimising
$\sum E_{imp}$	(MWh)	49.8	59.3
$\sum E_{exp}$	(MWh)	120.3	132.3
SCL	(%)	65.6	59.1

Table 4.5 shows a comparison of the annual differences in imported and exported power, and self consumption level. As expected, the amount of imported power is larger for the cost minimising strategy due to importing cheap power instead of using stored energy. This priority also lowers the SCL. The increase in exported power can also be explained by the fact that the controller prioritises grid prices over the battery content - the battery must be discharged in order to be charged again. If $SOC = SOC_{max}$, excess power must be exported to grid.

5

Dynamic controller

Once the control strategies have been tested using the hour based simulations, a set of three dynamic controllers will be implemented to investigate real-time performance. Since dynamic control requires much higher sample rate, the simulations will now only be done over a few seconds instead of a whole year.

5.1 General system model

Prior to implementing the controllers in MATLAB Simulink[®](Simulink[®]), the AWL system must be modeled by mathematical expressions. To simplify, the included physical components are narrowed down to the battery, DC-link and Energy hub. The solar panels, SSOs, load and ESOs will thus not be modeled. Instead the calculated remaining power, ΔP is seen as an input which will disturb the power balance in the system.

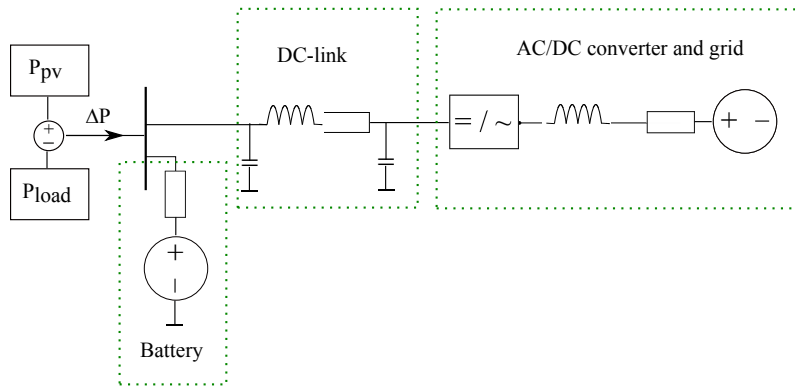


Figure 5.1: Overview of the AWL system components, used to implement Simulink[®]controllers and models of physical components.

Based on ΔP the three controllers will regulate to charge or discharge the battery, the DC-link voltage and grid power transfer. Figure 5.1 shows the AWL system layout, which is used to derive the mathematical models of physical components (battery, DC-link and grid) and the controllers. The DC-link and the battery models are mathematically derived in Sections 5.3.1 and Section 5.3.2 respectively. The grid model was not created during this thesis project and is explained further in Section 5.2.1.

to be more powerful than if the ESO would have been included.

5.2.1 Grid model

The main grid can be modeled as a voltage source behind an impedance. In AWL the connecting component is the Energy Hub, an AC/DC converter. The function of this component is to ensure that the power transfer between AWL and the grid is synchronized at all times. To enable this synchronized transfer, the grid voltage, current and frequency is measured and used to control duty cycle calculations for converting AC to DC.

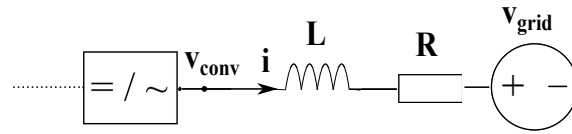


Figure 5.3: Equivalent circuit of an AC/DC converter connected to the main grid.

Figure 5.3 shows the equivalent circuit for modeling the main grid by above description. The voltage drop over the grid impedance can be found as

$$v_{conv} - v_{grid} = L \frac{di}{dt} + R i \quad (5.1)$$

and La Place transformation of (5.1) yields

$$v_{conv} - v_{grid} = i(sL + R). \quad (5.2)$$

The transfer function from the converter to the grid can then be found as

$$G(s) = \frac{Y(s)}{X(s)} = \frac{i}{v_{conv} - v_{grid}} = \frac{1}{(R + sL)}, \quad (5.3)$$

where R and L represent the resistance and inductance of the grid. In this thesis however, the grid and AC/DC converter is modeled using an existing model, as mentioned in Section 5.2. This is done to save time and simplify the implementation in Simulink®. The grid is now modeled as the electrical parts of a permanent magnet synchronous machine (PMSM), using the back EMF as the grid voltage meant to be balanced. This approximation is done to ensure that the grid can consume all the exported energy, and that it can generate the required energy for the AWL system. The voltage on the DC-link, V_{DC} , is used as an input to the AC/DC converter, the Energy Hub, resulting in grid currents, active and reactive power to the grid.

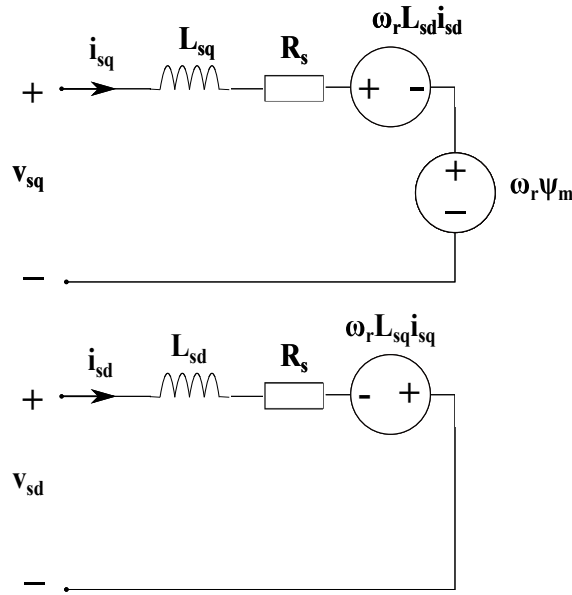


Figure 5.4: Equivalent circuit of a PMSM in dq -coordinates, used for modeling the grid. The back EMF is denoted as $\omega_r \psi_m$.

To simplify calculations, the voltage and currents are expressed using the dq -coordinate system. Where the voltage in dq -coordinates is found as

$$\begin{bmatrix} v_d \\ v_q \end{bmatrix} = \begin{bmatrix} \cos \theta & \sin \theta \\ -\sin \theta & \cos \theta \end{bmatrix} \begin{bmatrix} v_\alpha \\ v_\beta \end{bmatrix}, \quad (5.4)$$

and the transformation between $\alpha\beta$ and three phase.

$$\begin{bmatrix} v_\alpha(t) \\ v_\beta(t) \end{bmatrix} = \begin{bmatrix} \frac{2}{3} & \frac{-1}{3} & \frac{-1}{3} \\ 0 & \frac{1}{\sqrt{3}} & \frac{1}{\sqrt{3}} \end{bmatrix} \begin{bmatrix} v_a(t) \\ v_b(t) \\ v_c(t) \end{bmatrix}. \quad (5.5)$$

Where, $v_a(t)$, $v_b(t)$ and $v_c(t)$ are the phase voltages on the main grid,

$$\theta = \int \omega dt, \quad (5.6)$$

and $\frac{\omega}{2\pi}$ is the grid frequency [27]. Figure 5.4 shows the equivalent circuits of a PMSM in dq -reference frame. v_{sd} , v_{sq} , i_{sd} , i_{sq} , L_{sd} , L_{sq} and R_s are stator voltage, current, inductance and resistance. The back EMF is $\omega_r \psi_m$, where ψ_m is decided such that $\omega_r \psi_m$ is equal to the desired grid voltage. Using the equations for the stator voltage in a PMSM in dq -reference frame

$$\begin{cases} v_{sd} = R_s i_{sd} + L_{sd} \frac{di_{sd}}{dt} - \omega_r L_{sq} i_{sq} \\ v_{sq} = R_s i_{sq} + L_{sq} \frac{di_{sq}}{dt} - \omega_r L_{sd} i_{sd} + \omega_r \Psi_m \end{cases} \quad (5.7)$$

where ω_r is the rotor frequency. The grid frequency is modeled by resigning a fixed ω_r to match the grid frequency. Hence it is constant in the state space representation, which can be written as

$$\begin{bmatrix} \frac{di_{sd}}{dt} \\ \frac{di_{sq}}{dt} \\ \theta_r \end{bmatrix} = \begin{bmatrix} i_{sd} \\ i_{sq} \\ \omega_r \end{bmatrix} \begin{bmatrix} -\frac{R_s}{L_{sd}} & \frac{\omega_r L_{sq}}{L_{sd}} & 0 \\ \frac{-\omega_r L_{sd}}{L_{sq}} & \frac{-R_s}{L_{sq}} & -\psi_m \\ 0 & 0 & 1 \end{bmatrix} + \begin{bmatrix} v_{sd} \\ v_{sq} \end{bmatrix} \begin{bmatrix} \frac{1}{L_{sd}+R_s} & 0 \\ 0 & \frac{1}{L_{sq}+R_s} \end{bmatrix} \quad (5.8)$$

These are used in the s-function of the PMSM. To use the PMSM model as a grid model, the stator voltage represent the load side AC/DC voltage and R_s , L_{sd} and L_{sq} represent the grid impedance. Further, the mechanical parts of the machine are removed, hence the impact from mechanical torque, load torque and damping are removed.

Table 5.1: Parameters for grid model in dq-reference system.

Grid model parameters	Value	Unit
ω_r	2π50	(rad/s)
ψ_m	0.73	(Vs/rad)
L_{sd}	63.66	(mH)
L_{sq}	63.66	(mH)
R_s	20	(mΩ)

The parameters for the grid model are found in Table 5.1. Note that $L_{sd} = L_{sq}$ and that R_s is the same for both circuits in Figure 5.4.

5.2.2 AC/DC converter model

The Energy Hub is modeled by a model for an AC/DC converter and PWM module. Like the PMSM model in Section 5.2.1, no predecided parameters been altered. The assisting module performing the PWM however, has been slightly modified to fit the desired simulations by removing the impact of switching harmonics. In Simulink[®], this means choosing the PWM module to be analogue instead of based on sample and hold. This alteration saves simulation time, but harmonics in the output to the grid will not be detected. For this project however, the main interest is to see the dynamic response within the system. The quality of the exported power is therefore of less importance.

Table 5.2: Parameter for the AC/DC converter model.

AC/DC converter model	Value	Unit
C_{dc}	0.0024	(F)

The one parameter assigned to the AC/DC convert is a capacitance which is found in Table 5.2. This capacitance is used in the Simulink[®] model.

5.3 Derived models of physical components in Simulink[®]

In this Section the models which were derived during this thesis are presented. They include the DC-link, battery and battery SOC calculation. The DC-link is based on a Nexans DC cable [28] and the battery on the voltage-SOC characteristics of a suitable Nano phosphate cell [29].

5.3.1 DC-link model

The DC-link is located between the load and the Energy Hub in the Simulink[®] model. The remaining power deviation from $\Delta P = P_{PV} - P_{load}$ will cause an input current, ΔI which will disturb the voltage balance on the DC-link as it will create an increase of voltage across C_1 . This disturbance current is calculated by,

$$\Delta I = \frac{\Delta P}{V_{DC1}}. \quad (5.9)$$

where V_{DC1} is the load side of the DC-link which changes dynamically with the power input.

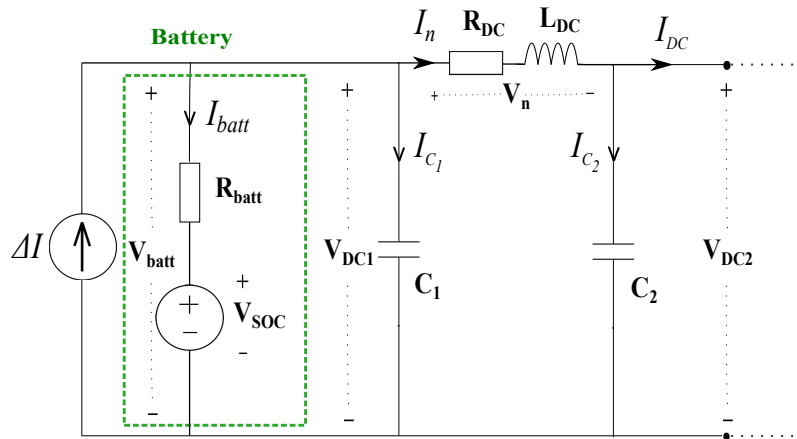


Figure 5.5: The equivalent circuit for the DC-link. Used to calculate differential equations need to model the DC-link.

The DC-link is modeled as a π -link which is shown in Figure 5.5. The parameters R_{DC} and L_{DC} were taken from a suitable Nexans DC-cable [28]. The capacitances C_1 and C_2 were put to match the capacitance of the preexisting model of the AC/DC converter [26]. From Figure 5.5 the equations for the dynamic model of the DC-link are derived as

$$\begin{cases} \frac{dV_{DC1}}{dt} &= I_{C1} = \frac{I_{\Delta P} - I_n - I_{batt}}{C_1} \\ \frac{dV_{DC2}}{dt} & I_{C2} = \frac{I_n - I_{DC}}{C_2} \\ \frac{dI_n}{dt} &= \frac{V_{DC1} - V_{DC2} - I_n R_{DC}}{L_{DC}}. \end{cases} \quad (5.10)$$

Using (5.10), the state space representation of the DC-link is

$$\begin{bmatrix} \frac{dV_{DC1}}{dt} \\ \frac{dV_{DC2}}{dt} \\ \frac{dI_n}{dt} \end{bmatrix} = \begin{bmatrix} V_{DC1} \\ V_{DC2} \\ I_n \end{bmatrix} \begin{bmatrix} 0 & 0 & \frac{-1}{C_1} \\ 0 & 0 & \frac{1}{C_2} \\ \frac{1}{L_{DC}} & \frac{-1}{L_{DC}} & \frac{-R_{DC}}{L_{DC}} \end{bmatrix} + \begin{bmatrix} I_{\Delta P} \\ I_{batt} \\ I_{DC} \end{bmatrix} \begin{bmatrix} \frac{1}{C_1} & \frac{-1}{C_1} & 0 \\ 0 & 0 & \frac{-1}{C_2} \\ 0 & 0 & 0 \end{bmatrix}. \quad (5.11)$$

These equations are the base for the Simulink[®]-model of the DC-link.

Table 5.3: Parameters of the DC-link model.

DC-link model parameters	Value	Unit
$l_{DC-link}$	63	(m)
R_{DC}	7.88	(mΩ)
L_{DC}	8.19	(μH)
$C_1 = C_2$	2.4	(mF)
V_{DCnom}	760	(V)
Allowed variation, ΔV_{DC}	760 ± 40	(V)

The parameters used for the DC-link model in Simulink[®] are listed in Table 5.3. Note that $C_1 = C_2$ and the allowed voltage interval of ΔV_{DC} .

5.3.2 Deriving the battery model

The battery is modeled by a voltage source, V_{SOC} and a series resistance, which represent the losses in the battery. The terminal of the battery is connected to the DC-link. The change in SOC is found by

$$SOC(t) = \int \left(\frac{100}{3.6 \cdot 10^6 E_{batt}} \right) P_{batt}(t) dt. \quad (5.12)$$

where SOC will be measured in percent and the power to the battery is

$$P_{batt}(t) = I_{batt}(t) V_{SOC}(t). \quad (5.13)$$

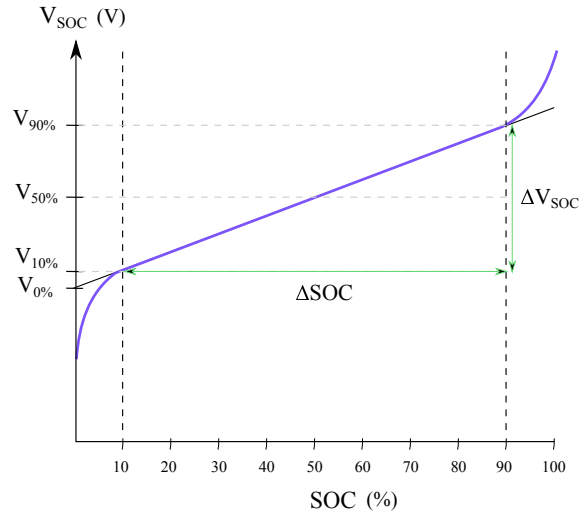


Figure 5.6: Approximation of the linear relation between V_{SOC} and SOC .

An example battery was used to create the battery model [29], Figure 5.6 shows the resulting voltage and SOC characteristics. Using the increase of voltage per SOC percentage, the linear voltage change between $SOC = 90\%$ and $SOC = 10\%$ can be described as

$$V_{SOC} = k SOC(t) + V_{0\%} \quad (5.14)$$

where k can be found as

$$k = \frac{\Delta V_{SOC}}{\Delta SOC}. \quad (5.15)$$

As can be seen in Figure 5.6, the characteristics of the battery is not entirely linear. However, as mentioned in Section 3.6, the DOD of the battery is constrained to range between SOC_{min} and SOC_{max} . This interval correlates well with the linear region of the example battery seen in Figure 5.6.

Table 5.4: Calculations of battery model parameters.

Parameters	Battery cell level	Battery model	Unit
Max. voltage	3.4	$3.4 n_{series}$	= 720.8 (V)
Nominal voltage	3.3	$3.3 n_{series}$	= 699.6 (V)
Max. charge current	100	$100 n_{parallel}$	= 2100 (A)
Pulse 10s charge current	200	$200 n_{parallel}$	= 4200 (A)
Max. discharge current	200	$200 n_{parallel}$	= 4200 (A)
Pulse 10s discharge current	600	$600 n_{parallel}$	= 12600 (A)
Nominal current	19.5	$19.5 n_{parallel}$	= 409.5 (A)
$V_{90\%}$	3.3	$720 - (k \cdot 10)$	= 712 (V)
$V_{10\%}$	3.0	$720 - (k \cdot 90)$	= 648.5 (V)
$V_{90\%} - V_{10\%} = \Delta V$	0.3	$0.3 n_{series}$	= 63.6 (V)
Internal resistance	$2.25 \cdot 10^{-3}$	$2.25 \cdot 10^{-3} n_{series}$	= 0.48 (Ω)
k	0.0038	$0.0038 n_{series}$	= 0.79 ($\frac{V}{\%}$)

The calculations used to set the battery parameters are found in Table 5.4 where $\eta_{series} = 242$ and $\eta_{parallel} = 19$. Note that the charge- and discharge current limitations are different, both for continuous current and sudden pulses.

5.4 Dynamic controllers in Simulink[®]

Three controllers were implemented in Simulink[®] using a cascaded setup. One current controller for grid power reference, one voltage regulator for maintaining the voltage on the DC-link within the required voltage limits, seen in Table 5.4, and finally one battery current controller.

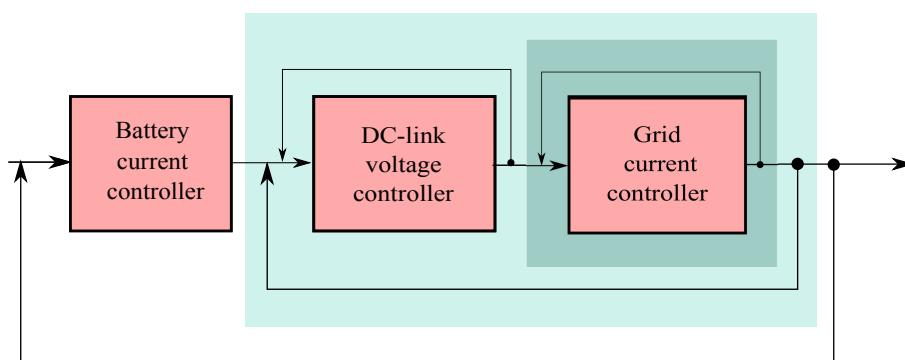


Figure 5.7: Overview of the cascaded control setup for the Simulink[®] implementation.

The cascaded control setup seen in Figure 5.7 was built in Simulink[®] from right to left. The speed requirements of each controller is dependent on the number of feedbacks it is included in. In this thesis, the grid current controller must be the fastest and the battery current controller the slowest.

5.4.1 Grid current controller

The power transfer between the AWL system and the grid is regulated by a current controller inside the AC/DC converter, the Energy Hub. A power reference is given by the DC-link voltage controller, described in Section 5.4.2, in order to regulate how much power should be exported or imported from the grid. This power reference is used to maintain voltage balance in the system. The Energy Hub measures the current and voltage on both the DC-link and the grid. These measurements are used to calculate control signals to a PWM module, ensuring that the exported current and voltage match the grid amplitude, frequency and phase angle. The grid current controller and the AC/DC converter model were based on a preexisting Simulink[®] system [30], [26]. The grid current control model was altered by calculating the current reference input from a power reference instead by

$$i_{sdq,ref} = P_{grid,ref} \frac{2}{3 \omega_r \psi_m} \quad [30]. \quad (5.16)$$

Where $P_{grid,ref}$ is the amount of power to be transferred to or from the grid for maintaining the DC-link voltage balance. Additionally, the switching harmonics from the PWM module were removed by changing the Simulink[®] settings to analogue. The changes resulted in faster simulations, but harmonics in the exported signals were undetectable. This adjustment is supported by the greater interest to observe the dynamic response inside the AWL system, than that of the main grid.

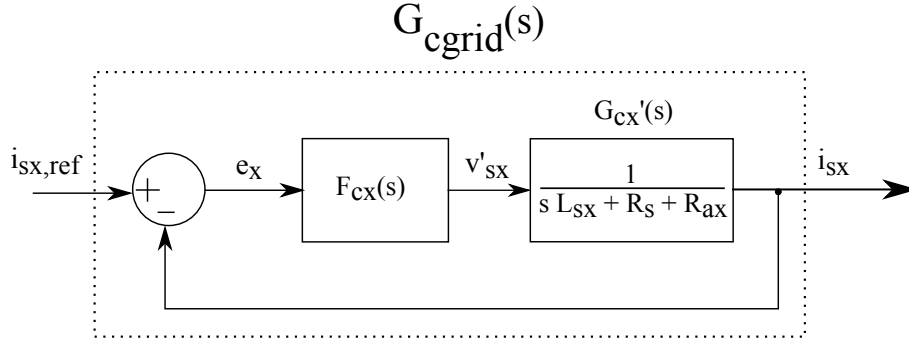


Figure 5.8: Schematics of the grid current controller. The index x can be exchanged for d or q to represent both signals in the dq -reference frame.

A block schedule over the grid current controller setup is shown in Figure 5.8 where the transfer function is found by La Place transforming and rewriting (5.8). Resulting in the equations needed for the current controller in dq -reference,

$$\begin{cases} i_{sd} = \frac{1}{L_{sd}s + R_s}(v_{sd} + \omega_r L_{sq} i_{sq}) = \frac{1}{L_{sd}s + R_s} v'_{sd} \\ i_{sq} = \frac{1}{L_{sq}s + R_s}(v_{sq} - \omega_r L_{sd} i_{sd} - \omega_r \psi_m) = \frac{1}{L_{sq}s + R_s} v'_{sq} \end{cases} \quad (5.17)$$

Adding an active damping term, R_a to enhance performance result in

$$\begin{cases} i_{sd} = \left(\frac{1}{L_{sd}s + R_s + R_a}\right)v'_{sd} = G_{cd}'(s)v'_{sd} \\ i_{sq} = \left(\frac{1}{L_{sq}s + R_s + R_a}\right)v'_{sq} = G_{cq}'(s)v'_{sq} \end{cases} \quad (5.18)$$

The gains for the PI controller F_{cx} is given by

$$F_{cx} = \frac{\alpha_{cr}}{s} G_{sx}'(s)^{-1} = \alpha_{cr} L_{sx} + \frac{\alpha_{cr}(R_{sx} + R_{ax})}{s} = K_{pcx} + \frac{K_{icx}}{s} \quad [27]. \quad (5.19)$$

Table 5.5: Parameters of grid current controller .

Parameters	Expression	Value	Unit
Bandwidth : α_{cr}	$(R_{sx} + R_{ax})/L_{sx}$	1000	(rad/s)
Active damping: R_{ax}	$\alpha_{cr} L_{sx} - R_{sx}$	0.63	(Ω)
Proportional gain: K_{pc}	$\alpha_{cr} L_{sx}$	0.64	
Integrator gain: K_{ic}	$\alpha_{cr}(R_{sx} + R_{ax})$	637	

The parameter indexes sx in Table 5.7 indicate d or q in the reference frame. However, grid current controller act on both i_{sd} and i_{sq} simultaneously. All parameters for this controller were taken from [30].

5.4.2 DC-link voltage controller

The power balance in the system is performed by maintaining the voltage over the DC-link to a reference value, V_{DCref} and to stay within the limits of 720 – 800 V. A voltage controller is to be implemented which, depending on the polarity of ΔP , will import or export the power difference. To simplify the controller, the physical DC-link model will be seen as a first order system consisting of one single capacitance, C . By doing so, the controller will interpret the DC-link as ideal, meaning that $R_{DC} \approx 0 \Omega$ and $L_{DC} \approx 0 mH$. Due to this assumption, $V_{DC1} \approx V_{DC2}$.

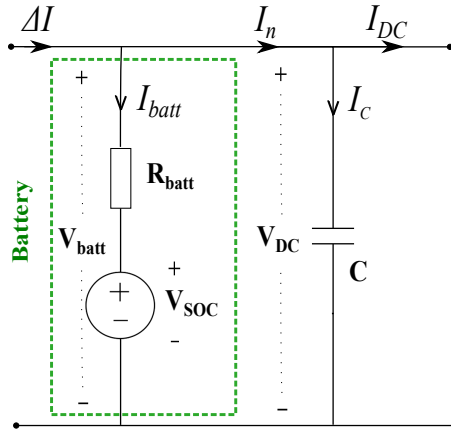


Figure 5.9: Equivalent circuit of the simplified DC-link previously seen in Figure 5.5, where $C = C_1 + C_2$ and $V_{DC} = V_{DC1} = V_{DC2}$.

The equivalent circuit of the controller view of the DC-link is shown in Figure 5.9. Important to remember is that although the voltage controller is implemented based on this simplified circuit, the actual physical model from Section 5.3.1 is much more complex. This will cause robustness issues for larger values of α_{vr} . The reason is that the small voltage drop across R_{DC} and L_{DC} will cause voltage oscillations between C_1 and C_2 , which will create a resonance circuit. The result will be that the step response of the voltage controller too will oscillate. In order to avoid disturbance from this behaviour, the voltage controller must be made slow enough not to detect the resonance in the DC-link voltage. In conclusion, for small values of α_{vr} , the voltage controller design based on interpreting the DC-link as a single capacitor will still give a satisfactory result. Starting from Figure 5.9, the energy in C is found as

$$E_c = \frac{C V_{DC}^2}{2}. \quad (5.20)$$

Where $V_{DC} = V_{DC1} = V_{DC2}$, and $C = (C_1 + C_2)$. The power to the capacitor, P_c is given by the derivative of E_c such that,

$$P_c = \frac{C}{2} \frac{dV_{DC}^2}{dt} \quad (5.21)$$

Fulfilling the constraint of power balance,

$$P_c = \Delta P - P_{batt} - P_{grid}, \quad (5.22)$$

where

$$\begin{aligned} P_{batt} &= V_{DC} I_{batt} = V_{DC} \left(\frac{V_{DC} - V_{SOC}}{R_{batt}} \right) \\ &\rightarrow P_{batt} = \frac{V_{DC}^2}{R_{batt}} - \frac{V_{DC} V_{SOC}}{R_{batt}}. \end{aligned} \quad (5.23)$$

For simplicity, the last term in (5.23) can be seen as a disturbance, using this assumption

$$P_{batt} \approx \frac{V_{DC}^2}{R_{batt}}. \quad (5.24)$$

Inserting into (5.21) yield

$$\frac{C}{2} \frac{dV_{DC}^2}{dt} + \frac{V_{DC}^2}{R_{batt}} = \Delta P - P_{grid} = P'_n \quad (5.25)$$

Laplace transformation and extraction of V_{DC}^2 from (5.25) yield,

$$V_{DC}^2 = \frac{2P'_n}{sC + \frac{1}{R_{batt}}} = \frac{P'_n}{\frac{sC}{2} + \frac{1}{R_{batt}}} \quad (5.26)$$

where $\frac{1}{R_{batt}}$ can be seen as an active damping of the voltage controller. Concluding the controller gains

$$\begin{aligned} F_v &= \frac{\alpha_{vr}}{s} G'_v(s)^{-1} = \frac{\alpha_{vr} C}{2} + \frac{\alpha_{vr}}{R_{batt} s} \\ &\rightarrow F_v = K_{pv} + \frac{K_{iv}}{s} \quad [27]. \end{aligned} \quad (5.27)$$

The bandwidth α_{vr} had to be smaller by a factor 10 than that of the grid current controller in Section 5.4.1. In addition, it must be slow enough not to perceive the voltage oscillations between C_1 and C_2 . Therefore, no mathematical derivation was made. Instead different values below 100 were tested. The results are shown in Figure 5.15.

Table 5.6: Parameters for the DC-link voltage controller.

Parameters	Expression	Value	Unit
Bandwidth : α_{vr}	Chosen, see Section 5.5.1	40	(rad/s)
Proportional gain: K_{pv}	$\alpha_{vr} \left(\frac{C}{2} \right)$	0.09	
Integrator gain: K_{iv}	$\alpha_{vr} \left(\frac{1}{R_{batt}} \right)$	$1.4 \cdot 10^3$	

Table 5.6 show the paramters for the DC-link voltage controller. Note that

$$\alpha_{vr} \ll \alpha_{cr}.$$

Finally, the neglection in (5.23) should be commented on. It is not entirely legitimate, since the removed disturbance has a V_{DC} dependency. However, the voltage

controller performance can be seen in Section 5.5 and it proves acceptable behaviour despite this simplification.

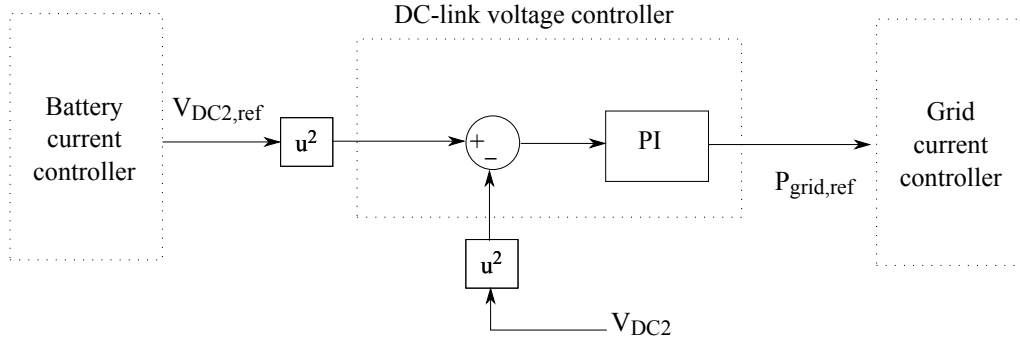


Figure 5.10: Block schedule for the DC-link voltage controller, showing the inputs and outputs.

The input and output to the DC-link voltage controller is shown in Figure 5.10. Note that the input reference $V_{DC,ref}$, is coming from the battery current controller and that the output, $P_{grid,ref}$ is the reference to the grid current controller.

5.4.3 Battery current controller

The battery SOC is dependent on the input or output of battery current,

$$I_{batt} = \frac{V_{DC1} - V_{SOC}}{R_{batt}} \quad (5.28)$$

assuming that V_{SOC} is a disturbance to the current regulator and putting $V_{SOC} = 0$ yield

$$I_{batt} = \frac{V_{DC1}}{R_{batt}} = G_{crb} V_{DC2} \quad (5.29)$$

Resulting in that the controller, F_{crb} is found as

$$F_{crb} = \frac{\alpha_{crb}}{s} G_{crb}^{-1} = \frac{\alpha_{crb}}{s} R_{batt} \quad (5.30)$$

where α_{crb} is the controller bandwidth.

Table 5.7: Parameters for the battery current controller.

Parameters	Expression	Value
Bandwidth : α_{crbatt}	Chosen	7 (rad/s)
Proportional gain: K_{pcbatt}	$\alpha_{crbatt} R_{batt}$	0.20

To ensure good performance,

$$\alpha_{crb} < \alpha_{vr} < \alpha_{cr}.$$

and since α_{vr} was tuned by testing different values, α_{crb} had to be chosen as based on the resulting α_{vr} .

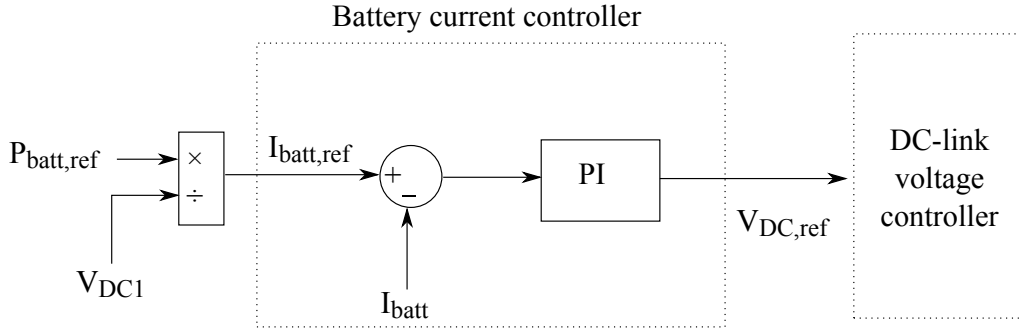


Figure 5.11: Block schedule for the battery current controller, showing the inputs and outputs.

A simplified block schedule representing the battery current controller is shown in Figure 5.11. Note that the input reference $I_{batt,ref}$, is calculated from the incoming battery power, however in the Simulink® model this reference is set manually. This enables $I_{batt,ref}$ to be independent of ΔI , which means that the battery can be charged regardless of access of solar power. The output from the battery current controller is the reference for the DC-link voltage controller. Which results in that the voltage controller will regulate based on the actions of the battery and import grid power to charge it, should the solar power not be enough.

5.5 Validation of implemented regulators

In this section the implemented controller are validated based on rise time t_r , steady state point, losses and how well each controller follows the reference when the whole system is in operation. Initial condition

Table 5.8: Initial conditions for all dynamic simulations

Parameter	Value	Unit	Parameter	Value	Unit
SOC	50	(%)	P_{exp}	0	(kW)
I_{batt}	0	(A)	P_{imp}	0	(kW)
ΔI	0	(A)	V_{DC1}	766	(V)
			V_{DC2}	766	(V)

5.5.1 Rise time

The rise time, t_r , of a first order system is defined as the time it takes for the system response to go from 10 – 90% of the step amplitude [31].

$$t_r = t_{r90\%} - t_{r10\%} \quad (5.31)$$

It can thereby be found graphically from the system step response. It is also dependent on the system bandwidth α . The dependence can be derived from

$$t_r = \frac{\ln(9)}{2\pi f_c}. \quad (5.32)$$

Where f_c is the cut-off frequency which is given by

$$f_c = \frac{1}{2\pi\tau} \quad (5.33)$$

Where τ is the time constant for the controller, related to the controller bandwidth, α as

$$\tau = \frac{1}{\alpha}, \quad (5.34)$$

Combining (5.31) and (5.34) show that the rise time to be related to the bandwidth by

$$t_r = \frac{\ln(9)}{\alpha}. \quad (5.35)$$

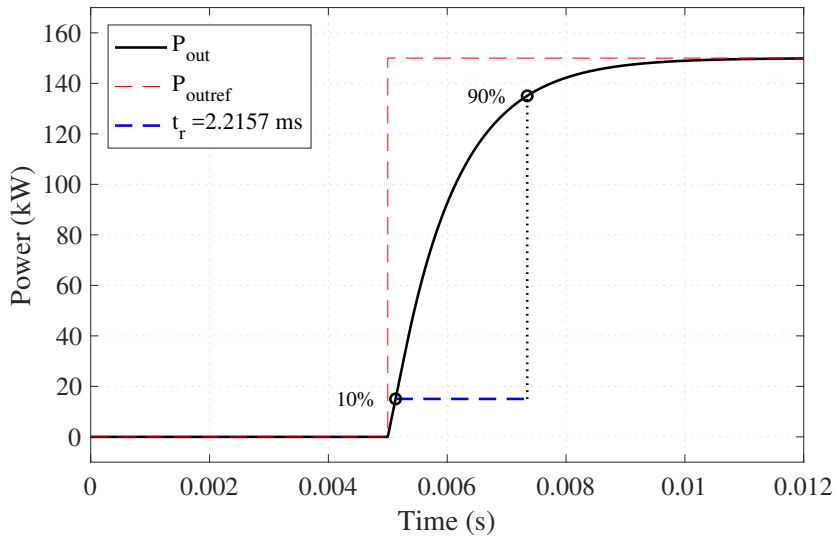


Figure 5.12: Step response for the grid current controller for a step of 150 kW. $\alpha_{cr} = 1000$ (rad/s)

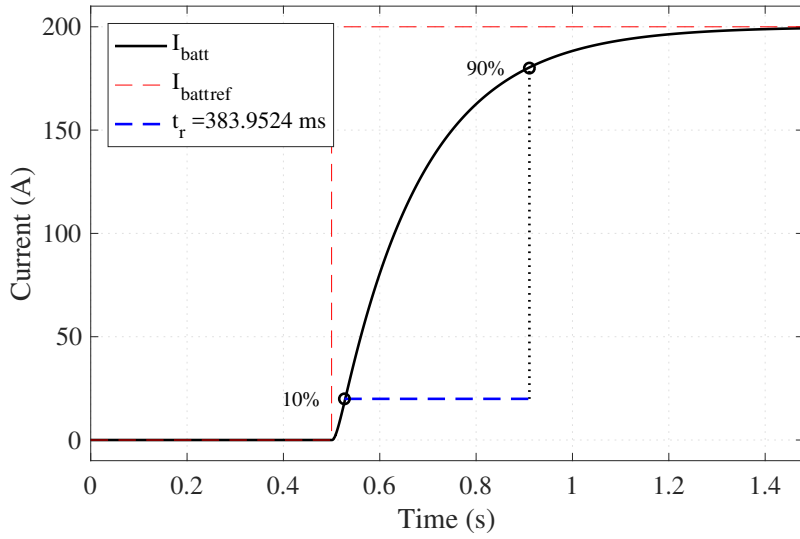


Figure 5.13: Step response for the battery current controller for a step of 200 A. $\alpha_{crb} = 7$ (rad/s)

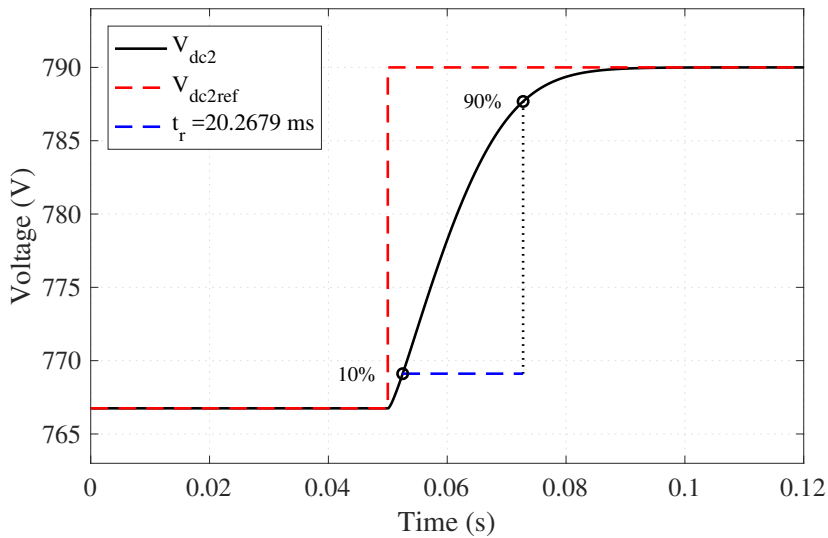


Figure 5.14: Step response for the DC-link voltage controller for a step up to 790 V. $\alpha_{vr} = 40$ (rad/s).

Figure 5.12 to Figure 5.14 show the rise times for all three controllers. Note the differences in t_r due to the requirement that

$$\alpha_{cbatt} < \alpha_{vr} < \alpha_{cr}.$$

has been met. As previously mentioned in Section 5.4.2, a large bandwidth for the voltage controller will cause stability issues.

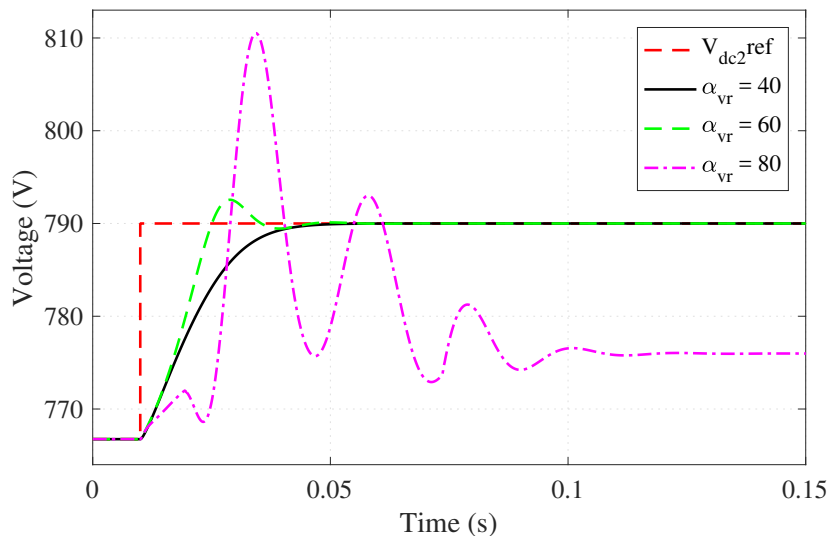


Figure 5.15: Step response for the voltage controller with different bandwidths, $\alpha_{vr} = 40, 60$ and 80 rad/s.

Figure 5.15 show the behavior of the voltage controller using different α_{vr} , as discussed in Section 5.4.2, the performance of the system is disturbed by the resonance issues for $\alpha_{vr} > 40$. Note the oscillations and inability to reach the reference for $\alpha_{vr} = 80$ and the overshoot when $\alpha_{vr} = 60$. The behaviour when $\alpha_{vr} = 60$ shows a second order response, which indicates that the voltage controller is too fast for the first order design to be acceptable. Since the voltage controller is the middle controller in the cascaded setup, (see Figure 5.7) its performance will be observable when overlooking the entire control system. Therefore, even though the response when $\alpha_{vr} = 60$ (rad/s) stabilized eventually, α_{vr} was chosen to be 40 (rad/s). When designing controller there is a trade off on speed and stability, here the more stable implementation was chosen.

Table 5.9: Bandwidth and rise time for the three implemented controllers

Controller	Bandwidth (rad/s)	Simulated t_r (ms)	Theoretical t_r (ms)
grid current	$\alpha_{cr} = 1000$	2.5	2.2
DC-link voltage	$\alpha_{vr} = 40$	20.3	54.9
Battery current	$\alpha_{crb} = 7$	388.5	314

As can be seen in Table 5.9, the theoretical rise times are faster than the actual rise times for all controllers. This can be explained by the fact that the line impedance of the DC-link is neglected in the DC-link voltage regulator, causing it to have a slightly lower gain than necessary. This will create a delay in the voltage regulator which will affect the entire system.

5.5.2 Power balance and losses

To detect losses in the system, an input step in input power was put to

$$P_{in} = \Delta P = 150 \text{ kW}$$

and output power was observed. The efficiency, η of the system is given by

$$\eta = \frac{P_{out}}{P_{in}} = \frac{I_{DC} V_{DC2}}{I_{\Delta P} \cdot V_{DC1}} \quad (5.36)$$

and the efficiency of the whole system was found to be $\eta = 0.9976\%$. To ensure that there are no unidentified losses in the system, the power loss in each physical component was evaluated. Concluding that the main losses were found in the battery and the DC-link impedance. From Figure 5.5

$$V_n = (I_{batt} R_{batt} + V_{SOC}) - V_{DC2} \quad (5.37)$$

making the power through the DC-link impedance

$$P_n = I_n V_n . \quad (5.38)$$

The power losses in the battery resistance is found as

$$P_{batt} = I_{batt}^2 R_{batt} . \quad (5.39)$$

Summing up the losses should be equal to,

$$P_{in} - P_{out} = P_{batt} + P_n . \quad (5.40)$$

Finally evaluation of the total input and output power is done by

$$\frac{P_{batt} + P_n + P_{out}}{P_{in}} = 1.000 . \quad (5.41)$$

Resulting in $\eta = 100$, showing that all system losses are found.

5.5.3 Manual test sequence

In this section, the controllers are tested by changing the input current, ΔI and the battery current reference, $I_{batt,ref}$. Important to remember is that ΔI is an uncontrollable input to the real system and serves as a disturbance to the voltage regulator. To keep the power balance, the voltage regulator will transfer the power difference to or from the grid based on $V_{DC,ref}$, which is provided by the battery current controller. From Section 5.4.3, the voltage reference is set by the battery current controller, which is controlled by a manual reference. When performing this test however, no real irradiance or load data was used, both ΔI and $I_{batt,ref}$ were set manually.

Table 5.10: Validation strategy for the dynamic controllers. The total simulation time is 3 s.

Step	Start	Signal	Amplitude	Expected results	Action
1	0.1s	ΔI	236 A	$P_{grid} > 0, I_{batt} = 0$	Export
2	0.5s	$I_{batt,ref}$	100 A	$P_{grid} > 0, I_{batt} > 0$	Export & charge
3	1.5s	ΔI	-386 A	$P_{grid} < 0, I_{batt} > 0$	Import & charge
4	2.0s	$I_{batt,ref}$	-150 A	$P_{grid} < 0, I_{batt} < 0$	Import & discharge

The expected validation results are shown in Table 5.10 and a brief explanation of each step follows

Step 1

A positive value of ΔI should cause an increase of the DC-link voltage, causing the voltage regulator to export the excess power to the grid. The current regulator for the battery however has not yet been given a reference, so it should remain at 0. The expected result of step 1 is therefore that all excess power should be exported to the grid.

Step 2

The battery current reference is changed and the battery should therefore start to charge, slightly decreasing the amount of exported power.

Step 3

A deficiency of power in the system is simulated, ΔI is negative. The voltage regulator should then import sufficient power to sustain both the load and the charging of the battery resulting in a negative P_{grid} but an unchanged battery current.

Step 4

$I_{batt,ref}$ is set to assist the grid by discharging the battery. Both I_{batt} and P_{grid} should then be negative, with a slight decrease of imported power. The results from the validation are shown in Figure 5.16 to Figure 5.20, where references are in dashed red and actual signals are in solid black.

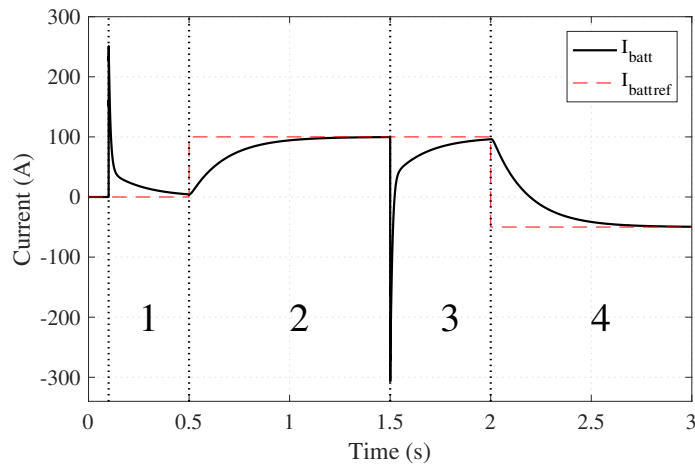


Figure 5.16: The battery current reference, $I_{batt,ref}$ and the actual battery current, I_{batt} .

The performance of the battery current controller can be seen in Figure 5.16. Note the peaks at $t = 0.1$ s and at $t = 1.5$ s, where ΔI cause a change of voltage over the DC-link. Since I_{batt} depend on V_{DC2} it affects the battery current even though $I_{batt,ref} = 0$. However, the regulator adjusts I_{batt} back to $I_{batt,ref}$. The negative peak can be explained in the same way, when ΔI suddenly is negative there is a drop in DC-link voltage which cause the battery current to drop as well. Again, the current regulator manages to restore I_{batt} back to $I_{batt,ref}$ showing that the battery current controller is working. One can also note that although the sudden current spikes undoubtedly are unhealthy for the battery, the current limits stated in Table 5.4 have not been breached.

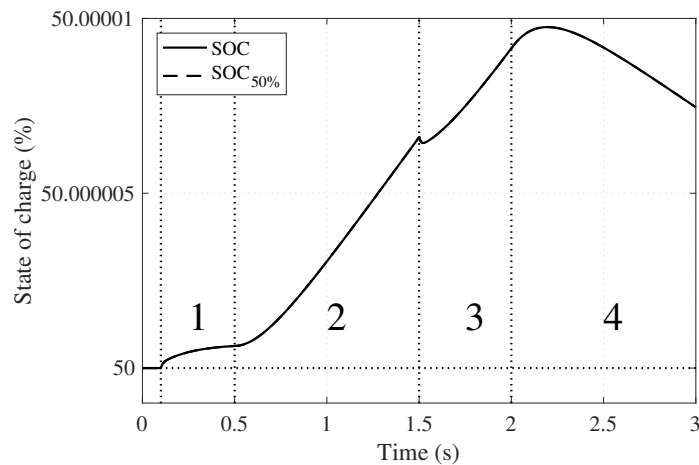


Figure 5.17: The alterations in SOC due to changes of the battery current, I_{batt} .

The impact of I_{batt} on the SOC of the battery can be seen in Figure 5.17. The simulation starts with the battery at $SOC_{50\%}$ and then there is a slow increase due

to the positive battery current. Once I_{batt} goes negative at $t = 1.5$ s there is a steady decrease of SOC instead. The slow changes in SOC can be explained by the size and charge rate of the battery. The battery capacity is 300 kWh and $Q_{max} = 100$ kW, meaning there will be very small changes during a simulation lasting only 3 seconds.

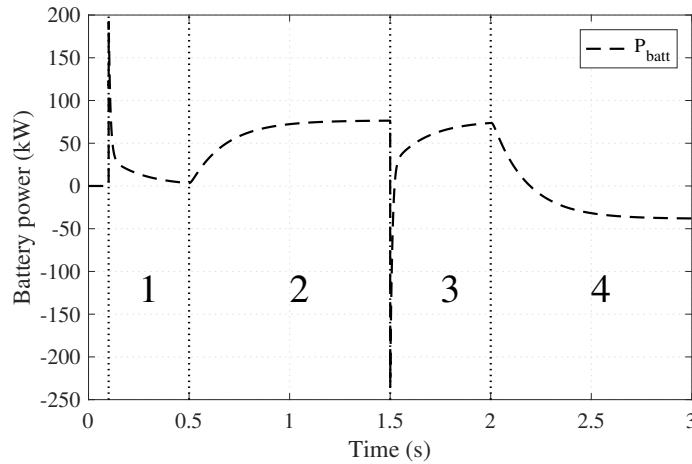


Figure 5.18: The power entering and exiting the battery, used to calculate SOC

Figure 5.18 shows the power in the battery. As expected the shape of the power curve is similar to I_{batt} in Figure 5.16. Worth noting is that the battery power is not limited by Q_{max} stated in Section 4.1.1 and increase above 200 A, when the peaks in I_{batt} are high.

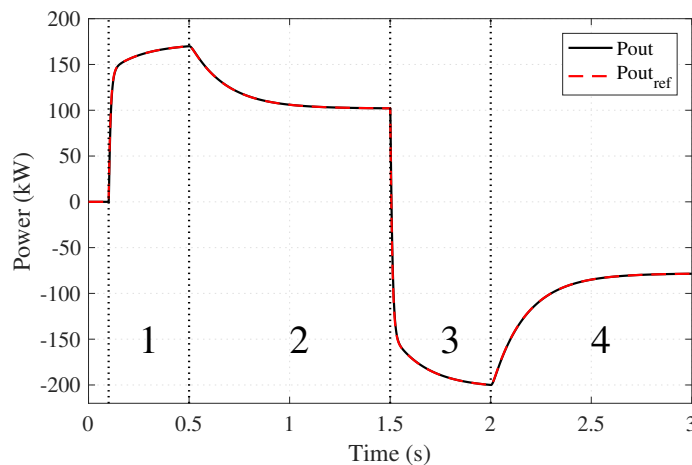


Figure 5.19: The power reference and the actual power transferred to and from the grid.

Figure 5.19 display the grid power exchange, where both section 1 and 2 show excess power being exported to the grid. During section 2 the exported power show a slight decrease due to the charging of the battery. In section 3 and 4 power is imported

from the grid. Again, due to the impact of the battery current the imported grid power is decreased once aided by the battery. The grid current controller is the fastest regulator in the system, and it can be seen in Figure 5.19 that it follows the reference very well.

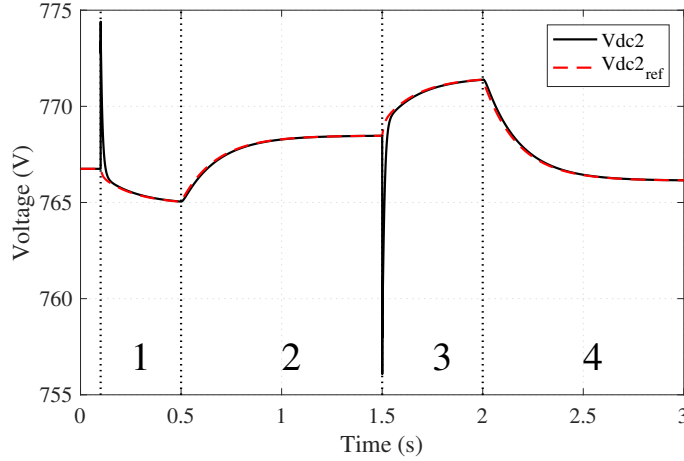


Figure 5.20: The DC-link voltage reference and the actual DC-link voltage

In Figure 5.20 however, similar peaks as in from Figure 5.16 can be noted. Also the voltage regulator deals with the disturbance from the injected ΔI and since $\alpha_{vr} > \alpha_{crb}$, the DC-link voltage is stabilised faster than the battery current. One can also note that the DC-link voltage is maintained within the allowed interval ΔV_{DC} , despite the disturbance. To compare, an example for how much the DC-link voltage would increase during 20 ms without a regulator is shown below.

Denote the power transferred to the DC-link during 20 ms as

$$P_{20ms} - P_{0s} = \Delta P$$

$$\Delta P = 100 \text{ A} \times 767 \text{ V} \times 0.020 \text{ s} = 1534 \text{ W s}.$$

Using (5.21) the voltage level after 20 ms is found by

$$\Delta P = \frac{1}{2} C (V_{DC,new}^2 - V_{DC}^2) = \frac{8 \cdot 10^{-3}}{2} C (V_{DC,new}^2 - 767^2)$$

Resulting in that the new voltage level would be

$$V_{DC,new} = \sqrt{\frac{2 \times \Delta P}{8 \cdot 10^{-3}} + 767^2} = 985.79 \text{ V}$$

if unregulated.

The voltage amplitudes of the peaks are then not harmful for the equipment connected to the DC-link. However, the swift changes might still cause problems.

5.5.4 Increase capacitance to lower battery current peaks

One way to decrease the peaks in I_{batt} caused by the injected ΔI is to increase the DC-link capacitance. This will cause slower change in V_{DC2} and hence affect I_{batt} in a similar way. Figure A.13 to Figure A.18 in Appendix show the result once the capacitances C_1 and C_2 have been increased by a factor 100. Note the much smaller peaks in I_{batt} , injecting current from the solar panels will now be much less traumatic for the battery. Although I_{batt} benefits from this alteration, capacitors are voltage stiff components and the result can be seen in Figure A.16. As the proportional gain $K_{pv} \propto (C_1 + C_2)$, the controller performance is now slower than before. Although the peak is smaller, the controller overshoots. The effect is also seen in Figure A.18, where the transferred power curve is much less smooth compared to Figure A.17. A better solution for this problem would be to model the ESOs, which serve as a DC/DC converter and separate the battery voltage from the DC-link voltage regulation. This would enable injection of current without risking damage to the battery.

6

Conclusions and Future work

In this Chapter the concluding results and possible future work will be presented.

6.1 Conclusions

A system consisting of solar panels, a DC microgrid was simulated in MATLAB® while ranging different battery sizes and using two control strategies for power flow. These simulations were done to determine the optimal battery size for the system, whilst meeting the Swedish governments goal of increasing the use of renewable energy. By controlling the power flow, the generated solar power supplied 65.6% of the total annual energy consumption. The battery storage was sized by evaluating the resulting grid interactions when the system was controlled by the strategy to maximise self-sufficiency. The optimal size was found to be 300 kWh and required a charge- and discharge rate of 100 kW to be able to supply the maximum load demand at any moment. Battery sizes larger than 300 kWh proved to be inefficient for the AWL system, as they did not increase self-sufficiency more than a few percent. Concluding that the solar power capacity and load consumption were the limiting factors of self-sufficiency during these simulations.

Two control strategies were implemented, both constrained to minimise losses, preserve battery life and to keep the power balance in the system. The first control strategy aimed to maximise the self-sufficiency, where implementation resulted in a self-sufficiency of 65.6%. Simulations of the AWL system using the strategy for self-sufficiency, and with battery sizes ranging from 0 – 500, proved that an energy storage in combination with this strategy could increase the self-sufficiency with up to 26.4%. The second control strategy aimed to minimise the operational cost of the system. This is done by controlling the system to import grid power if the electricity price was below the average price for that specific day, regardless of battery SOC. The implementation of this strategy resulted in a higher import than the previous strategy. Yet it still proved to be more cost efficient, since the grid imports occurred during low price hours. The implementation also resulted in a higher export of energy but a lower self-sufficiency due to the decrease of battery utilization.

Furthermore, a dynamic controller was implemented in order to investigate the behaviour of the system during real-time variations. A mathematical representation of the physical components was built in MATLAB Simulink®. The cascaded control setup consisted of three controllers: a grid current controller, a DC-link voltage

controller and a battery current controller. A sequence of events is constructed to test the response of the dynamic controllers, which show a good performance. It managed to keep the power balance in the system while charging and discharging the battery and transferring power to and from the main grid as desired.

6.2 Improvements and future work

Future implementations of similar projects could contain the following improvements.

Use second life batteries

To improve the environmental aspect of the project, second life batteries could be implemented in the system. This, is to investigate if the performance of the system is affected, and whether it is a more cost efficient solution. As the future market for second life batteries is growing rapidly, using them as stationary energy storages could be an interesting alternative.

Purchase renewable energy from the grid

Another way to meet the goal of increased use of renewable energy could be to only purchase renewable energy from the main grid. Today, this would increase the cost of the imported energy. However, this might be changed in the future in order to promote increased use of renewables.

Improve the cost minimising control strategy

To minimise the operational cost, the purchased grid power during low electricity price hours could be used to charge the battery. As the control strategies presented in this report aimed to minimise the losses in the system, the battery was never charged with grid power. It could however be a cost optimal solution. Since an empty battery during day-time forces the system to purchase energy from the grid regardless of electricity price. This could be beneficial during winter when the electricity price is high and the irradiance is very limited (in Sweden). Another improvement in the cost minimising strategy could be to evaluate the cost for each cycle in the battery. Meaning, finding the depreciation of the battery for each cycle. This would be interesting to know in order to investigate how low the price of purchased energy must be to compensate for the aging of the battery in each cycle.

Use faster sampling

Investigate if the result of the battery sizing and control strategies is improved by using a sample rate higher than 1 hour.

Investigate the battery sizing based on starting day

In all simulations during this project, the battery has started on SOC_{min} and the starting day has been the 1st of January. This resulted in that no battery, regardless of size, could enable the system to be 100% self-sufficient. It would be interesting to find the optimal starting day and SOC to reach 100% self-sufficiency before sizing

the battery storage.

Implement a predictive controller

Investigate if the self-sufficiency can be increased if a predictive controller is implemented. The controller should be taking tomorrows weather forecast into consideration and control the power flow with the possibility to save energy for the next coming days. The controller could also discharge the battery during low load hours if the forecast predicted a sunny day in the coming day.

Improvements of the dynamic controller

The dynamic controller can be improved in the following ways:

- Implement the control strategies from Section 3.6.
- Run the simulation using irradiance and load data.
- Implement constraints for $I_{batt,ref}$, such as limited to maximal charge rate, dependency of excess solar power.
- Include the efficiencies from Table 1.1 to the Simulink® model.
- Implement a DC/DC converter controlling the power flow to and from the battery.
- Design the DC-link voltage controller based on the actual physical model of the DC-link, not the simplified.

Include the AWL system in the FED project

Fossil free Energy District (FED) is a Chalmers initiative for selling or exchanging renewable energy between the buildings on campus, which the AWL building could be a part of. This gives the opportunity to sell excess power from AWL to other buildings on campus instead of the grid. Including the AWL system in FED also gives the opportunity to buy power from other parts of Chalmers and FED.

Bibliography

- [1] S. Government. Goals and visions. [Online]. Available: <https://www.government.se/government-policy/energy/goals-and-visions/>
- [2] G. Mulder, F. D. Ridder, and D. Six, “Global market outlook for photovoltaics 2014-2018,” *EPIA Report*, 2014.
- [3] B. Wunder, L. Ott, and M. Szpek, “Energy efficient dc-grids for commercial buildings,” in *Telecommunications Energy Conference (INTELEC), 2014 IEEE 36th International*. IEEE, 2014.
- [4] Etablera på Chalmersområdet, “A working lab på chalmersområdet,” 2018. [Online]. Available: <https://etablera.johannebergsciencepark.com/varfor-etablera-har/innovativa-byggnader/johanneberg-science-park-2/>
- [5] JinkoSolar, “Jkm280m-60.” [Online]. Available: <https://www.jinkosolar.com/ftp/EN-300M-60-PERC.pdf>
- [6] Ferroamp, “Ferroamp technology.” [Online]. Available: <http://www.ferroamp.com/>
- [7] B. Jernström, “Meeting at RI.SE on the 22nd of February, 2018.”
- [8] U.S. Department of Energy. The U.S. Department of Energy’s Microgrid Initiative. [Online]. Available: <https://www.energy.gov/sites/prod/files/2016/06/f32/The%20US%20Department%20of%20Energy%27s%20Microgrid%20Initiative.pdf>
- [9] H. Lotfi and A. Khodaei. AC versus DC microgrid planning. [Online]. Available: <http://ieeexplore.ieee.org.proxy.lib.chalmers.se/stamp/stamp.jsp?tp=&arnumber=7225166>
- [10] F. Zhang and *et al.*, “Advantages and challenges of dc microgrid for commercial building,” Institute of Solar Energy, College of Energy, Xiamen, Tech. Rep., 2015.
- [11] D. Fregosi *et al.* A comparative study of DC and AC microgrids in commercial buildings across different climates and operating profiles. [Online]. Available: <https://ieeexplore.ieee.org/stamp/stamp.jsp?tp=&arnumber=7152031>
- [12] Bosch BGT. American honda motor company – distribution center. [Online]. Available: <http://boschbgt.com/projects/american-honda-motor-company/index.html>
- [13] Hawaii Natural Energy Institute, University of Hawaii at Manoa. Moku o lo’e DC microgrid. [Online]. Available: <https://www.hnei.hawaii.edu/sites/www.hnei.hawaii.edu/files/CoconutIsland%20SPIDERS%20Luncheon%20HNEI%20L.Roose%20%288.27.15%29.pdf>
- [14] J. Groot, “State-of-health estimation of li-ion batteries: Cycle life test methods,” Ph.D. dissertation, Chalmers University of Technology, 2012.

- [15] M. S. Whittingham, “Lithium batteries and cathode materials,” <http://pubs.acs.org/doi/full/10.1021/cr020731c>, (Accessed on 12/12/2017).
- [16] E. Raszmann, K. Baker, Y. Shi, and D. Christensen, “Modeling stationary lithium-ion batteries for optimization and predictive control,” National Renewable Energy Laboratory, Tech. Rep., 2017.
- [17] M. Petit, E. Prada, and V. Sauvant-Moynot, “Development of an empirical aging model for li-ion batteries and application to assess the impact of vehicle-to-grid strategies on battery lifetime,” *Applied Energy*, vol. 172, pp. 398–407, 2016.
- [18] J. Groot, M. Swierczynskic, A. I. Stanc, and S. KnudsenKærc, “On the complex ageing characteristics of high-power lifepo4/graphite battery cells cycled with high charge and discharge currents,” *Journal of Power Sources*, vol. 286, pp. 475–487, 2015.
- [19] M. Günther, *Advanced CSP Teaching Materials*. DLR, Deutsches Zentrum für Luft- und Raumfahrt, 2012, ch. Chapter 2 Solar Radiation, pp. 16–31.
- [20] R. P. Paras Loomba, Sonal Asgotraa. Dc solar microgrids — a successful technology for rural sustainable development. [Online]. Available: <https://ieeexplore-ieee-org.proxy.lib.chalmers.se/document/7556601/authors>
- [21] T. Eram and P. L. Chapman, “Comparison of photovoltaic array maximum power point tracking techniques,” *IEEE TRANSACTIONS ON ENERGY CONVERSION*, vol. 22, no. 2, pp. 439–449, 2007.
- [22] Vattenfall, “Timpris på elbörsen,” January 2018. [Online]. Available: <https://www.vattenfall.se/elavtal/elpriser/rorligt-elpris/timpris-pa-elborsen/>
- [23] NordPool. Day-ahead prices. [Online]. Available: <https://www.nordpoolgroup.com/Market-data1/Dayahead/Area-Prices/>
- [24] The World Bank Group. Global solar atlas. [Online]. Available: <http://globalsolaratlas.info/?c=58.462102,12.082214,8&s=57.803798,11.90094>
- [25] MathWorks, “Lowess smoothing,” Matlab version R2017b. [Online]. Available: <https://se.mathworks.com/help/curvefit/lowess-smoothing.html>
- [26] Department of Energy and environment Chalmers University of Technology, “Field oriented control of ac machines home assignments and computer tasks 1 to 7,” 2017.
- [27] L. Harnefors, *Control of Variable-Speed Drives*. Mälardalen University Västerås, 2002.
- [28] Nexans, “Cable dimension of AXQJ 1 kV 3X240/72.” [Online]. Available: https://www.nexans.se/eservice/Sweden-sv_SE/navigateproduct_540327046/15152998.html#characteristics
- [29] A123 Energy Solutions, “Battery pack design, validation and assembly guide usig a123 systems amp 20m1hd-a nanophosphate cells.” 2014. [Online]. Available: http://www.formula-hybrid.org/wp-content/uploads/A123_AMP20_battery_Design_guide.pdf
- [30] Department of Energy and environment, Chalmers University of Technology, “Field oriented control of ac machines home assignments and computer tasks 1 to 7,” 2017.
- [31] C. Nordling and J. Österman, *Physics Handbook for Science and Engineering*. Carl Nordling and Jonny Österman and Studentlitteratur, 1980, 2006.

A

Appendix 1

Simulink

Here are snapshots of the entire Simulink model divided into respective subblocks. Each subblock is presented in subchapters with the same names as in this overview.

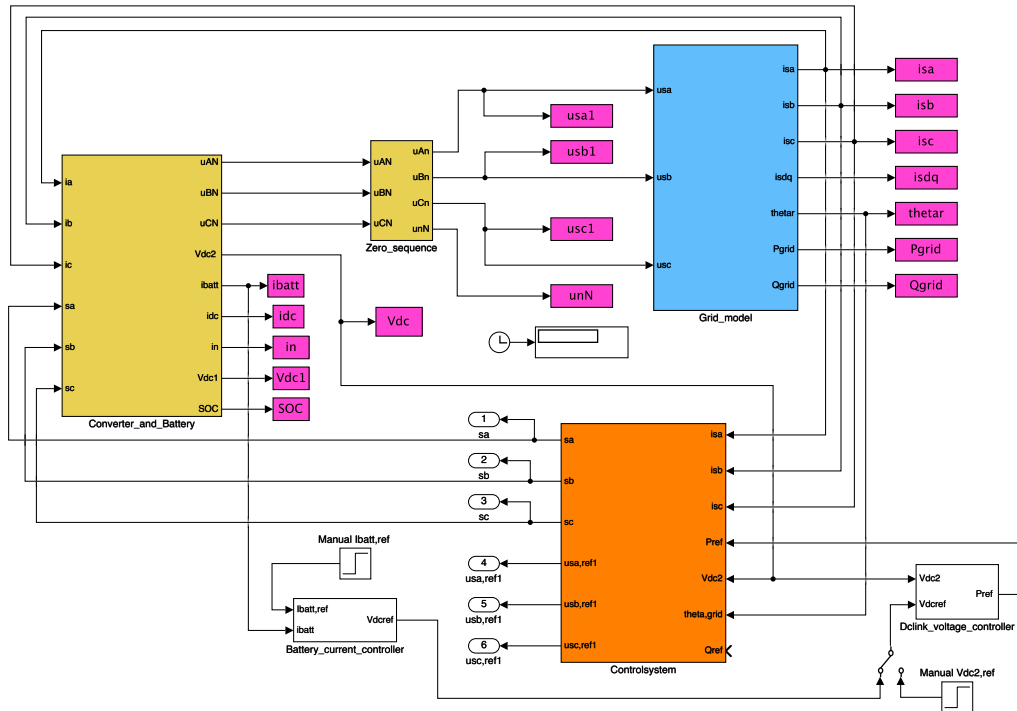


Figure A.1: The entire Simulink model used to model the AWL system. The signals in individual squares represent signals sent to MATLAB® workspace.

Control system

The control system contains the grid current reference calculation block, the AC/DC converter to grid current controller, the PWM module and duty cycle calculations. Taken from previously existing model [26], [30]. Modified by removing the switching harmonics by using the PWM module in analogue mode.

A. Appendix 1

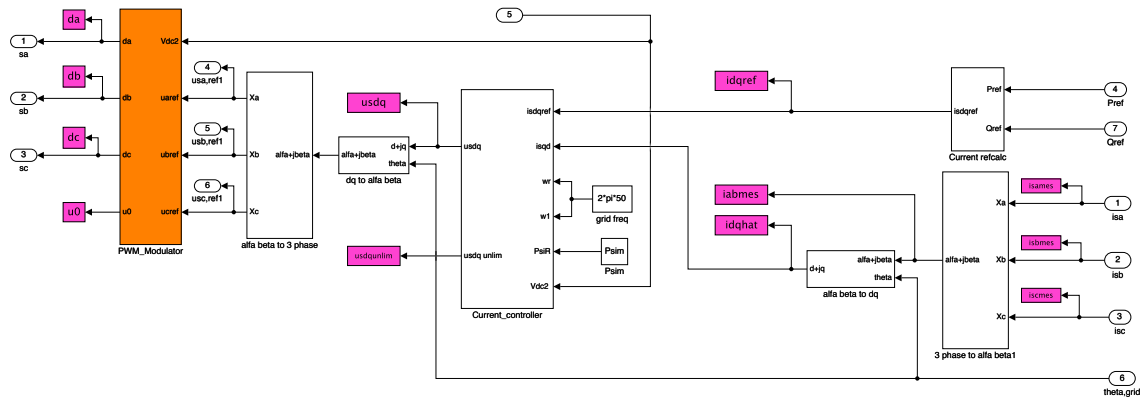


Figure A.2: Control system containing the PWM module and current controller for the grid.

Current reference calculation

Modified by changing the reference to originate from the power reference coming from the DC-link voltage controller (shown in Figure A.11), instead of from the measured grid current. Located inside the top right block shown in Figure A.2

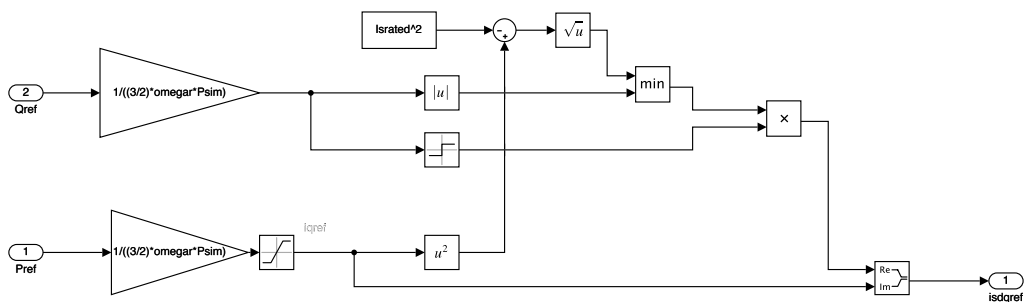


Figure A.3: Current reference calculation block, for the grid current controller.

Current controller

Located in the central block in Figure A.2.

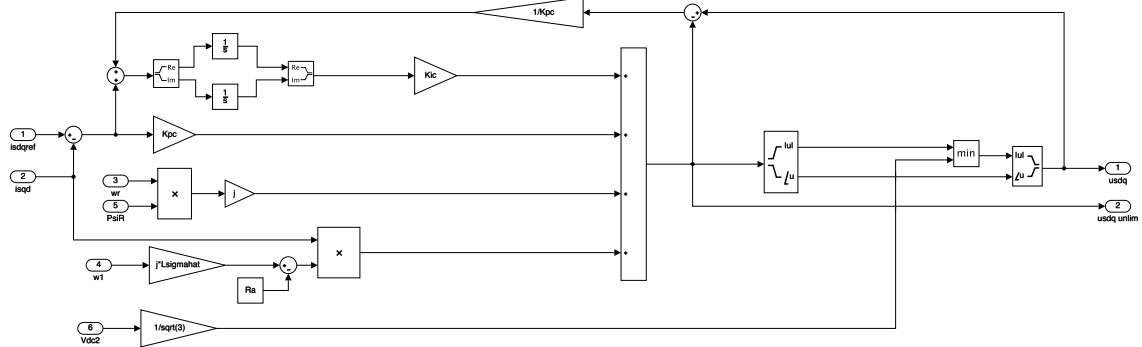


Figure A.4: Grid current controller, used for regulating the current sent from the DC-link to the grid model.

PWM module and duty cycle calculations

Located in the far left block in Figure A.2.

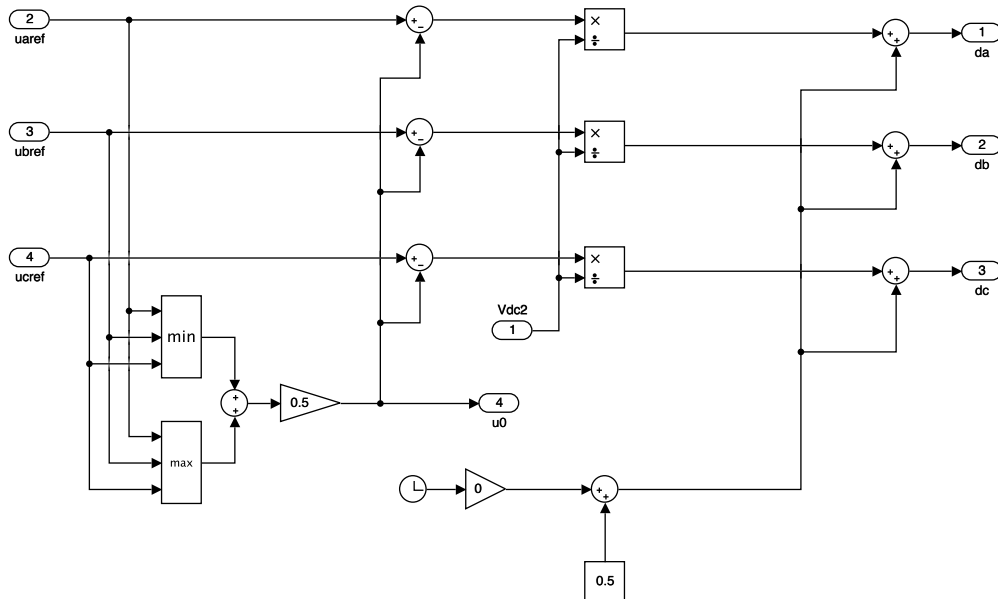


Figure A.5: PWM module used for calculating the duty cycle for the grid current.

Converter and battery

This subblock contains the physical models of the DC-link, battery and AC/DC converter. The AC/DC converter was taken from previously existing model [26],

[30]. The physical models of DC-link, battery and battery SOC model were derived during this thesis project.

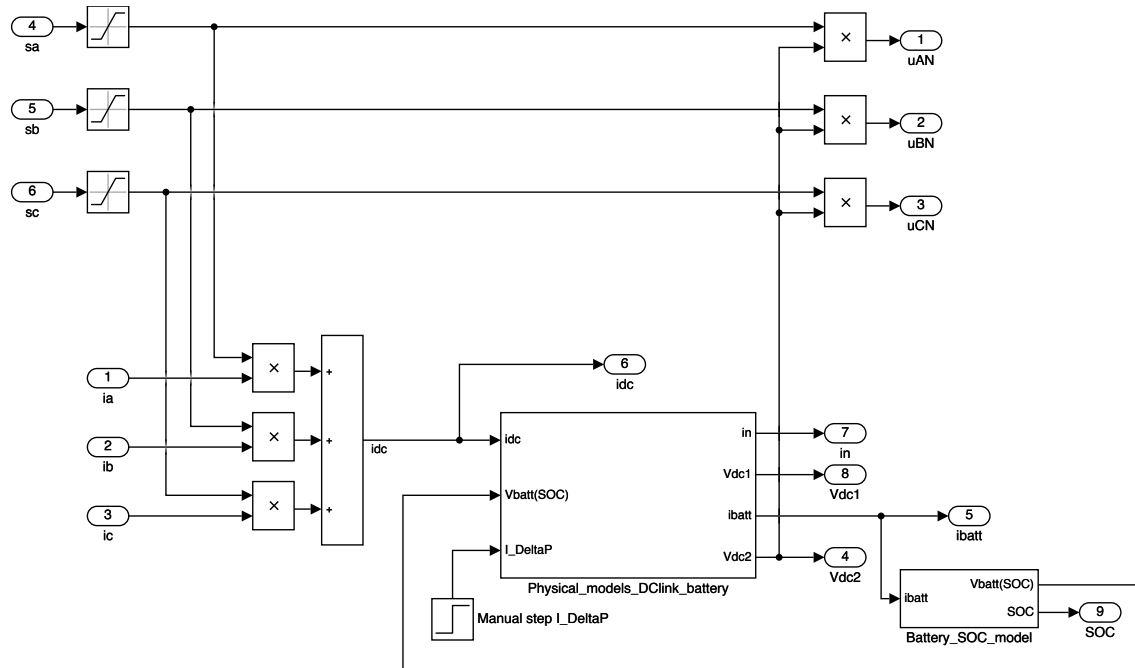


Figure A.6: Physical model of the AC/DC converter and the sub-system which contains the physical models of DC-link and battery.

The duty cycle from Figure A.5 are used to shape the current which needs to be supplied from the DC-link to match the existing grid current. Based on this current, the conditions on the DC-link will change.

DC-link and battery models

Located inside the large, central block in Figure A.8.

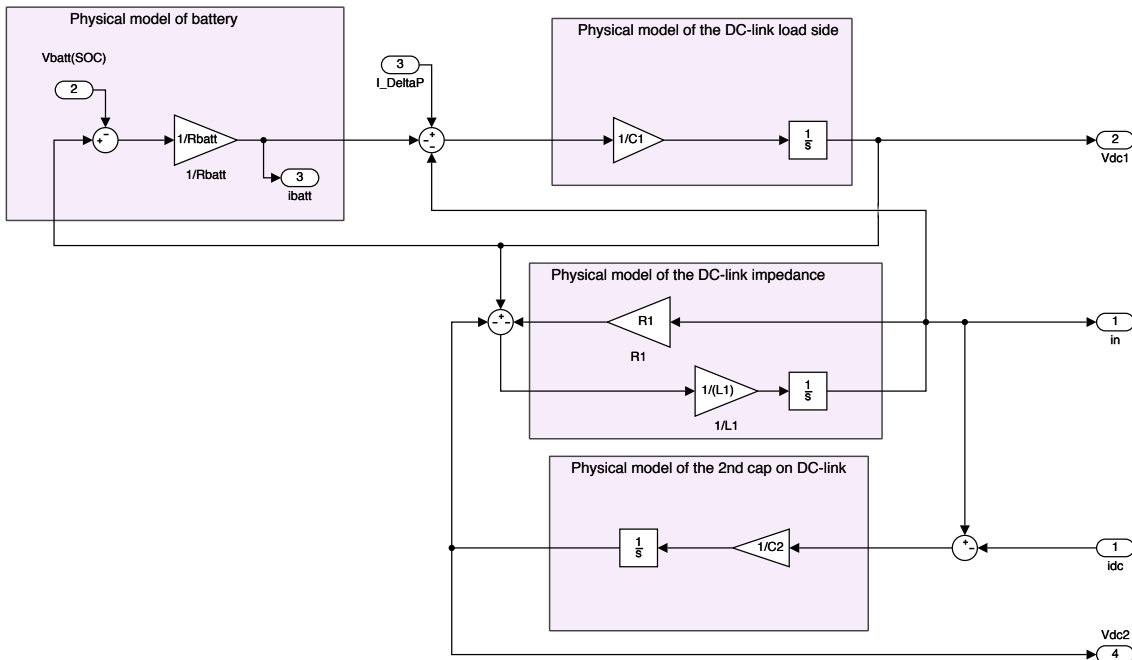


Figure A.7: The physical models of DC-link and battery.

SOC calculations

Located in the far right block in Figure A.8.

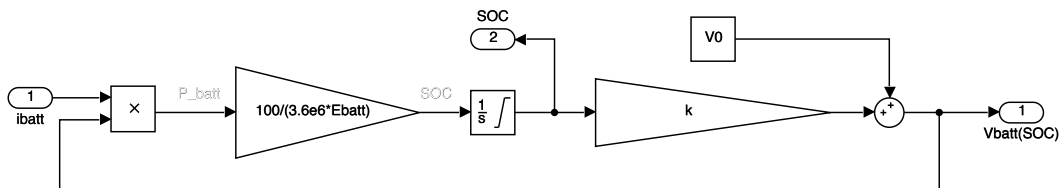


Figure A.8: Calculation of battery SOC based on the battery current $ibatt$ and the current battery voltage $V_{batt}(SOC)$.

Zero Sequence

Taken from previously existing model [26], [30]. Located in the small, center block in Figure A.1.

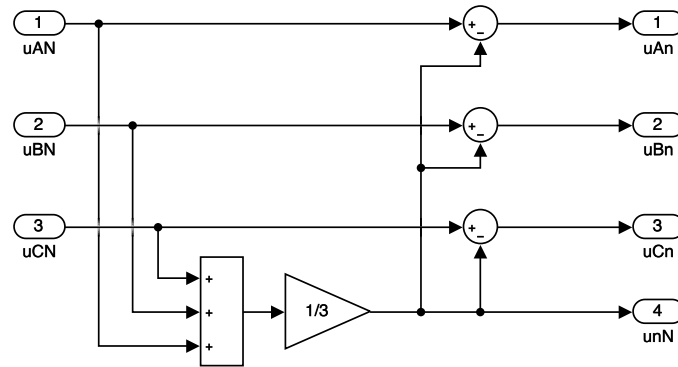


Figure A.9: The Zero sequence block alters the common neutral point of the grid voltage.

Grid model

Taken from previously existing model [26], [30]. Located in the top right block in Figure A.1. Altered according to previous description in Section 5.2. Contains the physical model of the grid and the s-function is based on Equation 5.8.

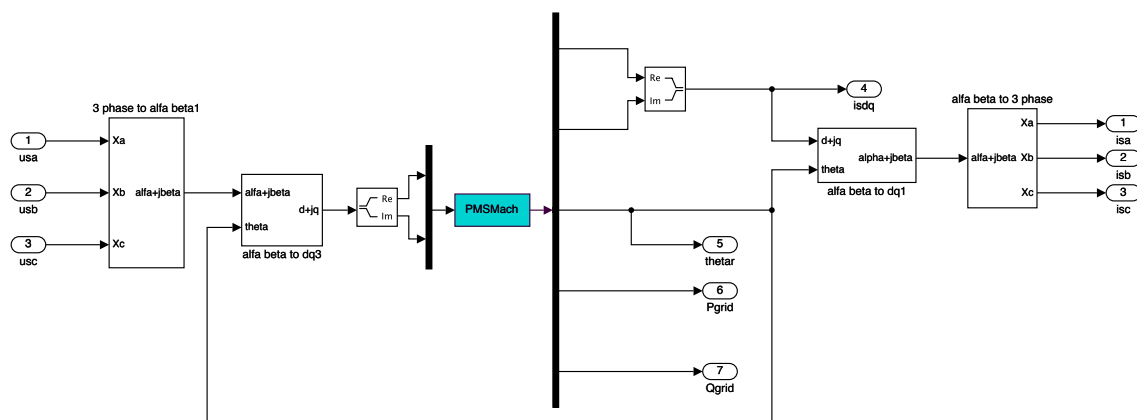


Figure A.10: Grid model in Simulink

DC-link voltage controller

Here the DC-link voltage controller block is presented. This controller was derived and implemented during this thesis project. Located in the bottom right block in Figure A.1. Note that in Figure A.1 the reference can be set manually or taken from the Battery current controller in Figure A.12.

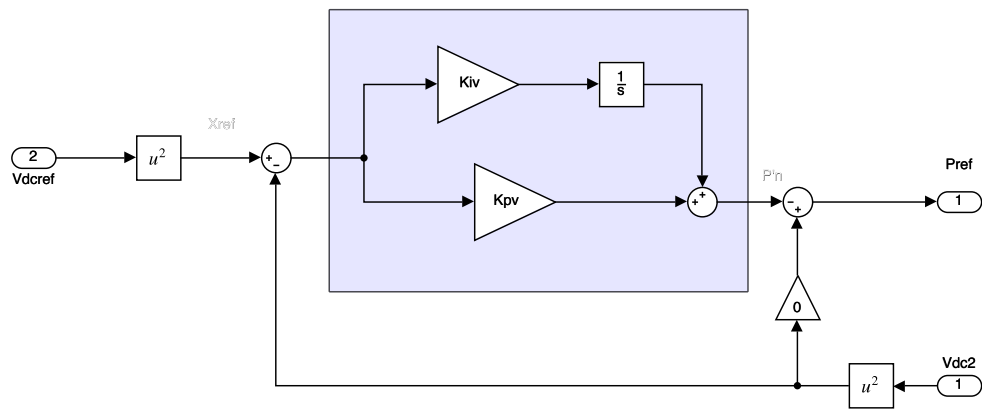


Figure A.11: DC-link voltage controller in Simulink

Battery current controller

Here the battery current controller is presented. This controller was derived and implemented during this thesis project. Located in the bottom left block in Figure A.1. Note that the reference for the battery current is set manually, as shown in Figure A.1.

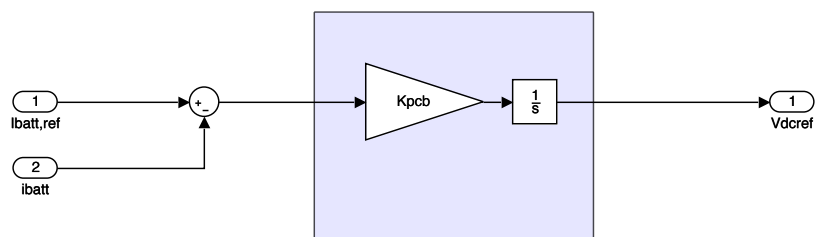


Figure A.12: Battery current controller in Simulink.

Controller performance $C = 100C1$

Table A.1: Validation strategy for dynamic controllers. Total simulation time is 3s.

Step	Time [s]	Signal	Amplitude [A]	Expected results
1	0.1	$I_{\Delta P}$	236	$P_{grid} > 0, I_{batt} = 0$
2	0.5	$I_{batt_{ref}}$	100	$P_{grid} > 0, I_{batt} > 0$
3	1.5	$I_{\Delta P}$	-386	$P_{grid} < 0, I_{batt} > 0$
4	2	$I_{batt_{ref}}$	-150	$P_{grid} < 0, I_{batt} < 0$

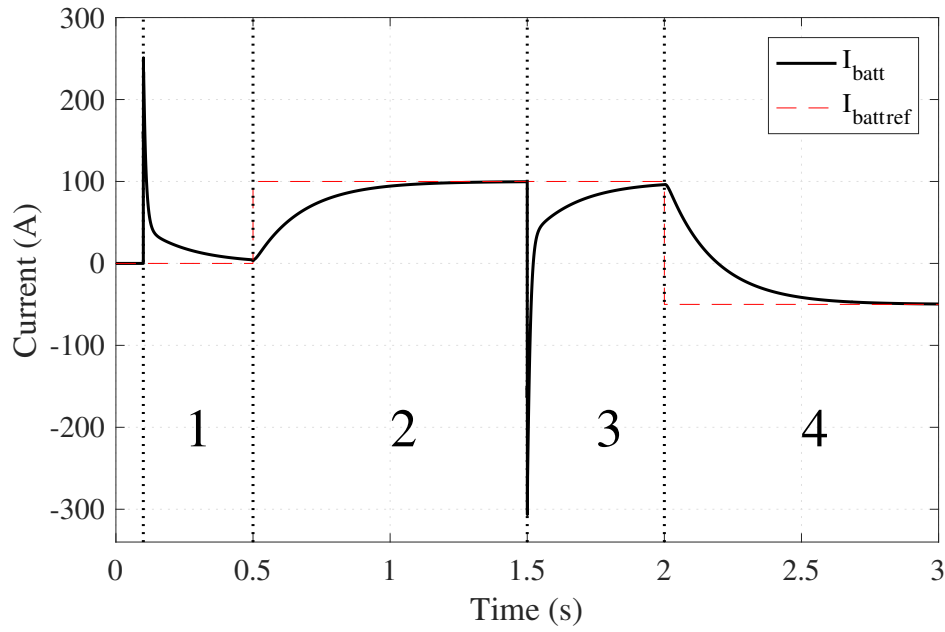


Figure A.13: The performance of the battery current controller when $C = C_1$.

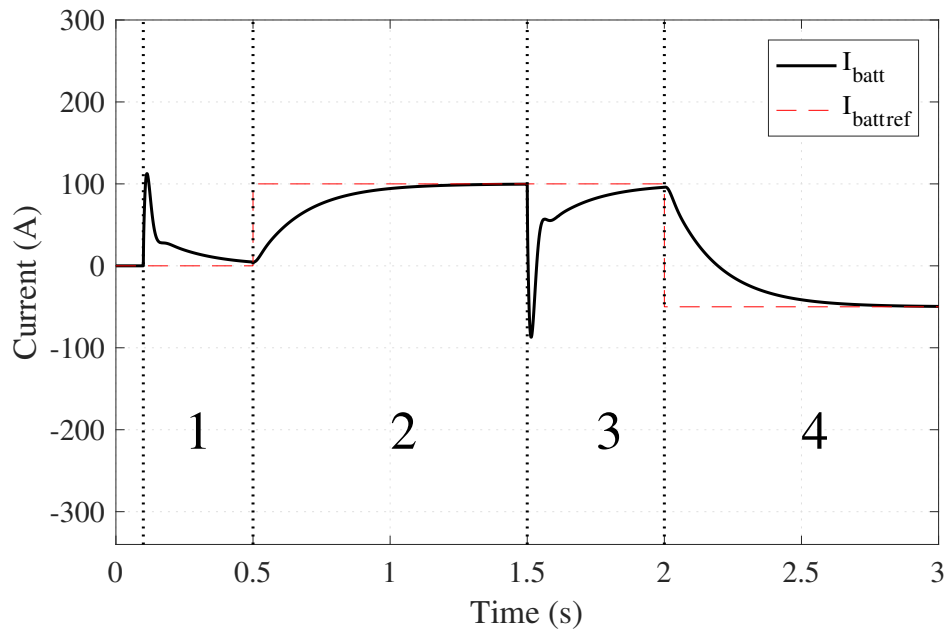


Figure A.14: The performance of the battery current controller when $C = 100C_1$.

VOLTAGE

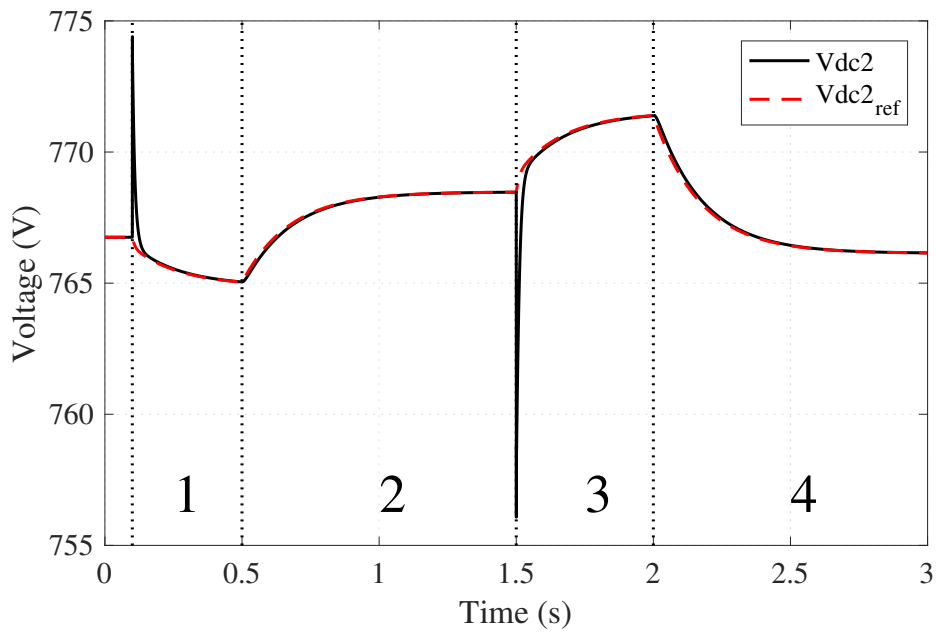


Figure A.15: The performance of the DC-link voltage controller when $C = C_1$.

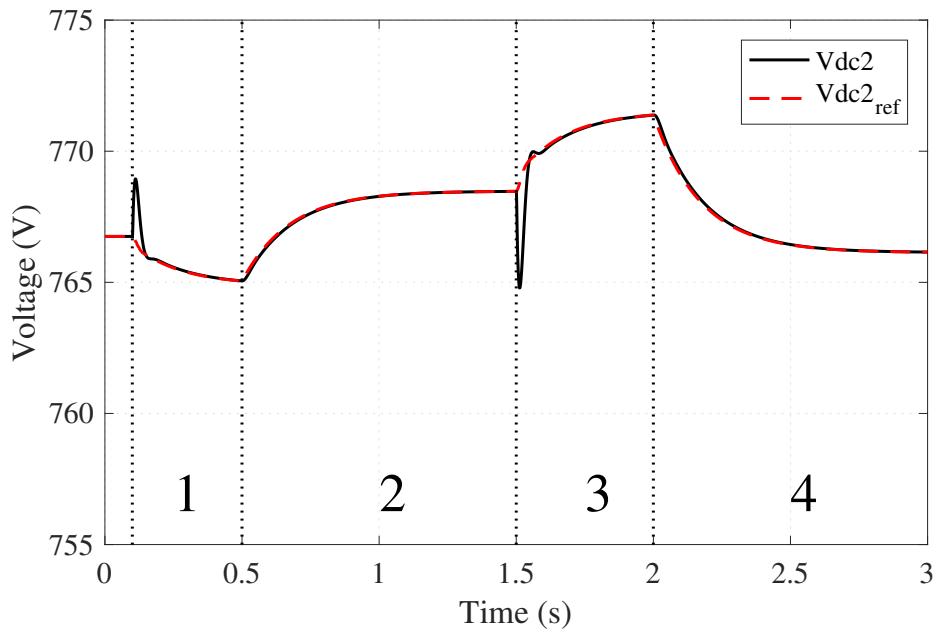


Figure A.16: The performance of the DC-link voltage controller when $C = 100C_1$.

POWER

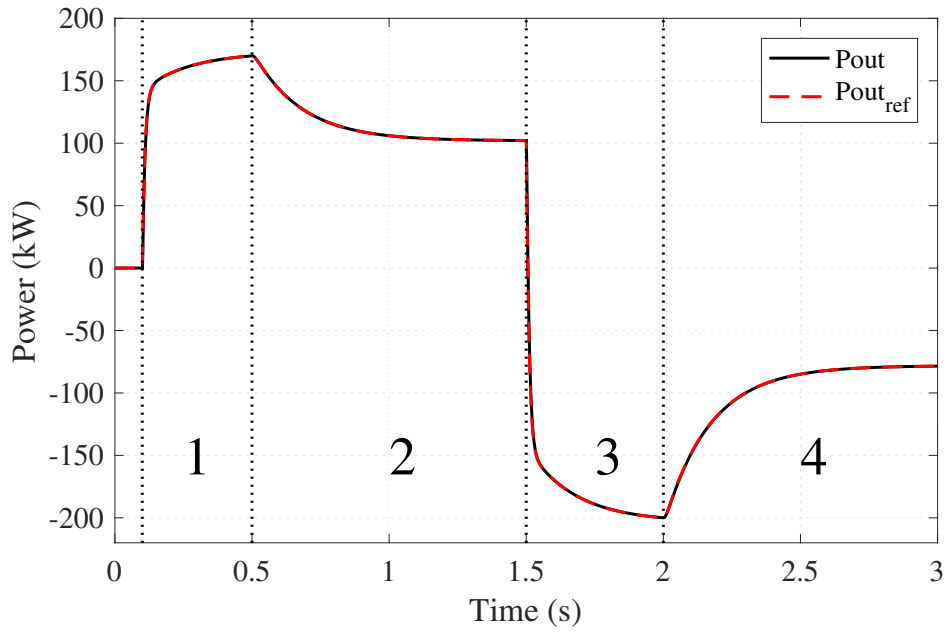


Figure A.17: The performance of the grid power current controller when $C = C_1$.

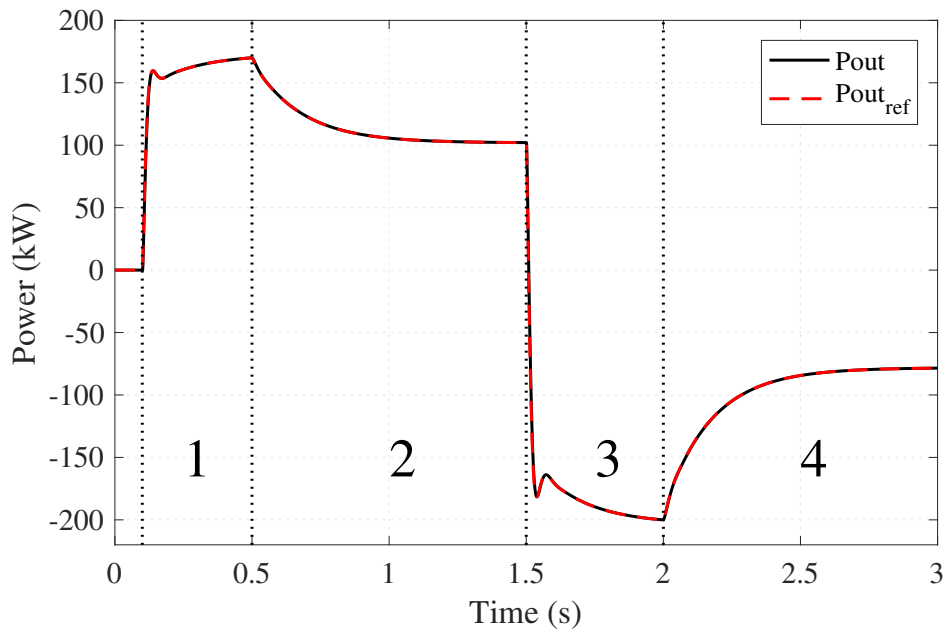


Figure A.18: The performance of the grid power current controller performance when $C = 100C_1$.